

Instability of rotating Bose stars

A.S. Dmitriev,^{1,2,*} D.G. Levkov,^{2,3,†} A.G. Panin,^{2,4,‡} E.K. Pushnaya,^{1,5,§} and I.I. Tkachev^{2,6,¶}

¹*Lomonosov Moscow State University, Faculty of Physics, Moscow 119991, Russia*

²*Institute for Nuclear Research of the Russian Academy of Sciences, Moscow 117312, Russia*

³*Institute for Theoretical and Mathematical Physics, MSU, Moscow 119991, Russia*

⁴*Moscow Institute of Physics and Technology, Dolgoprudny 141700, Russia*

⁵*University of Cambridge, DPMMS, Cambridge CB2 1TN*

⁶*Novosibirsk State University, Novosibirsk 630090, Russia*

(Dated: 08/06/2021)

Light bosonic (axion-like) dark matter may form Bose stars — clumps of nonrelativistic Bose–Einstein condensate supported by self-gravity. We study rotating Bose stars composed of condensed particles with nonzero angular momentum l . We analytically prove that these objects are unstable at arbitrary $l \neq 0$ if particle self-interactions are attractive or negligibly small. They decay by shedding off the particles and transporting the angular momentum to the periphery of the system until a Saturn-like configuration appears: one (or several) spin-zero Bose stars and clouds of diffuse particles orbit around the mutual center. In the case of no self-interactions we calculate the profiles and dominant instability modes of the rotating stars: numerically at $1 \leq l \leq 15$ and analytically at $l \gg 1$. Notably, their lifetimes are always comparable to the inverse binding energies; hence, these objects cannot be considered long-living. Finally, we numerically show that in models with sufficiently strong repulsive self-interactions the Bose star with $l = 1$ is stable.

I. INTRODUCTION AND MAIN RESULTS

Every object in the Universe can rotate around its center of mass and carry angular momentum. There is, however, a unique substance — Bose–Einstein condensate of particles in a quantum state $\psi(t, \mathbf{x})$ — that does not rotate easily, and if does, rotates in its own peculiar way. Indeed, the condensate velocity can be identified [1] with the phase gradient divided by the particle mass¹

$$\mathbf{v} = \nabla \arg \psi(t, \mathbf{x})/m .$$

This vector is explicitly irrotational at nonzero density: $\text{rot } \mathbf{v} = 0$ at $\psi \neq 0$. Hence, the only way to add rotation is to drill a hole through the condensate, i.e. introduce a vortex line $\psi = 0$ in Fig. 1. And this costs energy! As a by-product, the angular momentum of the condensate is quantized with the number l of vortex lines.

In the present-day Universe, the Bose–Einstein condensate of dark matter particles may exist in the form of gravitationally self-bound Bose stars [2–4], cf. [5]. During decades, the studies of these objects were migrating from the periphery of scientific interest towards its focal point [6]. Now, it is clear that the Bose stars may form abundantly by universal gravitational mechanisms [7–9] in the mainstream models with light dark matter. If the latter consists of QCD axions, they nucleate [9, 10] inside the typical axion miniclusters [11, 12] — widespread

smallest-scale structures conceived at the QCD phase transition [12–17]. In the case of fuzzy dark matter, gigantic Bose stars (“solitonic cores”) appear in the centers of galaxies during structure formation [8, 18, 19]. In both cases these objects cease growing beyond certain mass [10, 18, 20].

One can rotate the Bose star by drawing a vortex through its center. A stationary and axially-symmetric Ansatz of this type is [21–23]

$$\psi_s(\mathbf{x}) = \psi_s(r, z) e^{-i\omega_s t + il\varphi} , \quad (1)$$

where (r, φ, z) are the cylindrical coordinates, $\omega_s < 0$ is the binding energy of the condensed particles, and l is their angular momentum. The total spin of the Bose star is then $J_z = lM_s/m$, where M_s is its mass. Importantly, regularity requires ψ_s to vanish as r^l at $r \rightarrow 0$. Thus, the symmetry axis of the configuration (1) is indeed a vortex line with the winding number l .

Solving numerically the coupled equations for ψ_s and its gravitational potential, we obtain the profile of the rotating Bose star. It has a distinctive toroidal form, see Fig. 2 and cf. [22, 23].

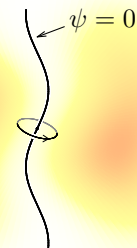


FIG. 1. (Not to scale) Bose–Einstein condensate (shaded region) rotating around the vortex line $\psi = 0$ (solid).

* dmitriev.as15@physics.msu.ru

† levkov@ms2.inr.ac.ru

‡ panin@ms2.inr.ac.ru

§ qutorcle@gmail.com

¶ tkachev@ms2.inr.ac.ru

¹ Units with $\hbar = 1$ are used in all dimensionful expressions.

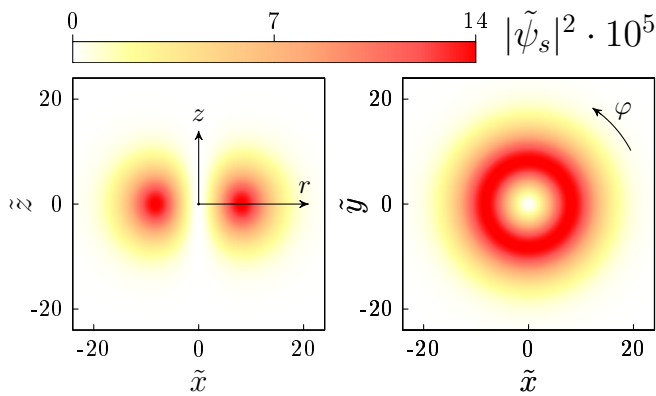


FIG. 2. Bose star (1) rotating with $l = 1$ around the z axis. This configuration is computed numerically in the case of negligible particle self-interactions, $\lambda = 0$. Left and right panels show $y = 0$ and $z = 0$ sections of the density profile $|\psi_s(\mathbf{x})|^2$, respectively. Tildes above the letters indicate dimensionless units (to be introduced in the main text).

Rotating Bose stars, if stable, would be important for astrophysics and cosmology. Their centrifugal barriers can resist [24, 25] to bosenovos — collapses of overly massive stars due to attractive self-interactions of bosons [26–28]. This means, in particular, that fast-rotating QCD axion stars would reach larger masses and densities [29] which may be sufficient to ignite observable parametric radioemission [4, 29–32], see the analytic analysis of the latter process in [33]. Besides, the angular momenta of the Bose stars are detectable in principle: directly by observing gravitational waves from their mergers [34–36] or indirectly if they eventually collapse into spinning black holes [2, 3] which merge and emit gravitational waves.

Surprisingly, none of the existing simulations show nucleation of the rotating objects (1) from generic Cauchy data, even if strong spherical asymmetry is present from the start. We numerically observed spin-zero Bose stars form [7–10, 20], collide [18], merge [30, 37, 38], or tidally disrupt [39, 40]. In the end of the simulations, they were strongly oscillating [19, 41, 42], random-walking [42, 43], partially or completely destroyed [18, 40], but never acquired a nonzero angular momentum. In addition, relativistic cousins of rotating Bose stars — the lumps of complex scalar field with $U(1)$ conserved charge bounded by Einstein gravity — were numerically shown to develop remarkable axially asymmetric instabilities [44–46].

All of this strongly suggests that rotating nonrelativistic Bose stars are unstable, although skeptics still may argue that some of the observed numerical instabilities could be artificially inflicted by the Cartesian lattices breaking axial symmetry. Besides, relativistic Bose stars — even at zero spin — have essentially different stability properties [4, 47] in phenomenologically interesting cases of QCD axions and axion-like particles as compared to the models with global $U(1)$ symmetry [44–46].

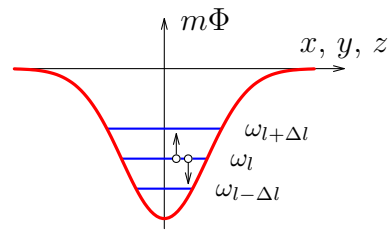


FIG. 3. (Not to scale) Instability of the rotating Bose star.

Executive summary

Let us summarize the main results and approaches leaving their derivation and technical details to the main text.

In this paper we analytically prove a no-go theorem: nonrelativistic gravitationally bound Bose stars (1) with arbitrary nonzero angular momentum are unstable in models with negligibly small ($\lambda = 0$) or attractive ($\lambda < 0$) particle self-interactions. This result is applicable in the popular cases of fuzzy and QCD axion dark matter. On the other hand, in models with repulsive self-interactions ($\lambda > 0$) a stability region for the $l = 1$ Bose star exists.

Our approach reveals the mechanism for the instability: it is caused by the pairwise transitions of the condensed particles from the original state with the angular momentum l to the $l + \Delta l$ and $l - \Delta l$ states, see Fig. 3. This process conserves the total spin and decreases the potential energy of the Bose star. Piling up due to Bose factors, the particle transitions lead to exponential growth of the axially asymmetric perturbations:

$$\delta\psi \propto e^{\mu t}, \quad (2)$$

where μ is the complex exponent and $(\text{Re } \mu)^{-1}$ is the lifetime of the rotating configuration (1).

In Fig. 4 we visualize three-dimensional numerical evolution of the perturbed $l = 1$ Bose star, see also the movie [48a] and cf. [44–46]. The panels (a)–(f) display horizontal sections of the solution at fixed time moments. The simulation starts in Fig. 4a with the star profile distorted by an invisibly small asymmetric perturbation $\delta\psi \sim 10^{-6}\psi_s$. The latter grows exponentially with time, becomes discernible at the moment of Fig. 4b and reaches a fully nonlinear regime $\delta\psi \sim \psi_s$ in Fig. 4c. At this point, a bound system of two spherical Bose stars appears. They oscillate and rotate around the mutual center of mass in Figs. 4c–e. Finally, one of the stars gets tidally disrupted, whereas the other survives. The evolution ends in Fig. 4f with nonspinning Bose star surrounded by a cloud of diffuse axions. They rotate around the mutual center of mass.

We explicitly compute the dominant instability modes of the rotating Bose stars in the case of purely gravitational interactions ($\lambda = 0$): numerically at moderately small l and analytically at $l \gg 1$. We also identify the angular momentum transfers Δl in the respective par-

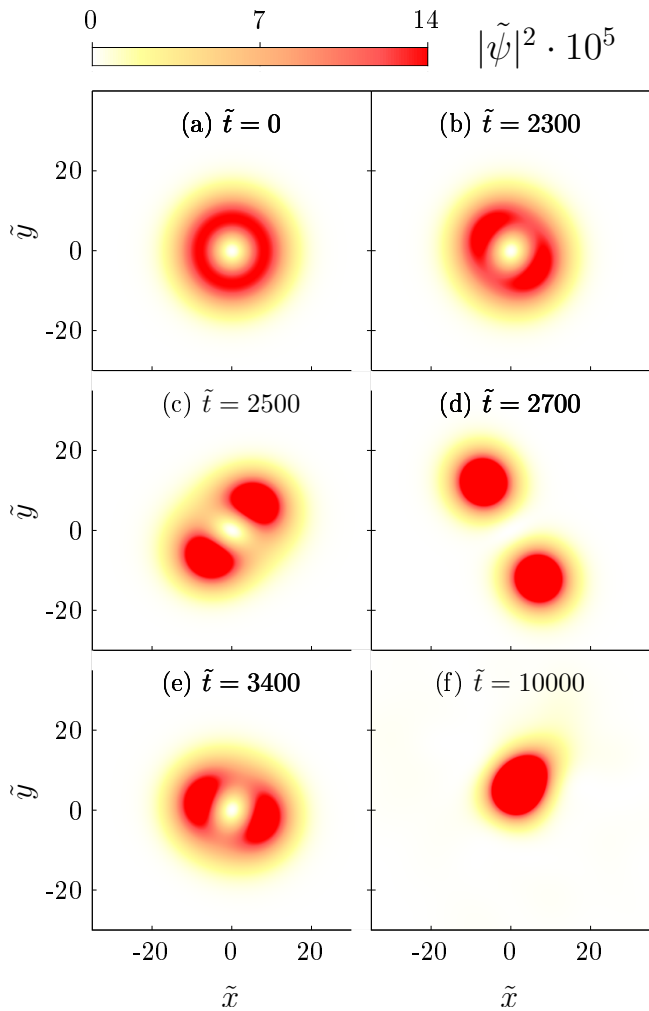


FIG. 4. Numerical evolution of the $l = 1$ Bose star in the case of purely gravitational interactions $\lambda = 0$, see [48a] for the related movie. Frames (a)–(f) display horizontal ($z = 0$) sections of the density $|\tilde{\psi}|^2$ at different times. Units are specified in the main text.

ticle transitions. In physical units, the complex growth exponents of the instability modes have the form,

$$\mu = \tilde{\mu} m^3 G^2 M_s^2, \quad (3)$$

where the dimensionless parameter $\tilde{\mu}$ and integer Δl depend only on l . Their numerical values are listed in Table I and displayed in Fig. 5 (circles).

At $l \gg 1$ and $\lambda = 0$ the parameters Δl and $\tilde{\mu}$ can be obtained analytically:

$$\begin{aligned} \Delta l &\approx [0.944 \cdot l / \sqrt{\alpha_l}], \\ \tilde{\mu} &\approx (2.22 - 2.39 i \sqrt{\alpha_l}) \cdot 10^{-2} \alpha_l / l^2, \end{aligned} \quad (l \gg 1) \quad (4)$$

with corrections suppressed by l^{-1} . Here $[\cdot]$ denotes the closest integer and order-one parameters α_l satisfy non-

l	Δl	$\text{Re } \tilde{\mu} \cdot 10^3$	$\text{Im } \tilde{\mu} \cdot 10^3$	l	Δl	$\text{Re } \tilde{\mu} \cdot 10^3$	$\text{Im } \tilde{\mu} \cdot 10^3$
1	2	7.73	-16.2	2	1	3.05	-9.64
3	3	2.42	-6.82	5	4	1.41	-3.45
7	5	0.91	-2.12	10	6	0.55	-1.13
15	8	0.29	-0.58	$\gg 1$	Eq. (4)		

TABLE I. Parameters of the dominant instabilities in rotating Bose stars with different l : angular momentum transfers Δl and complex growth exponents μ , see Eqs. (2), (3). The case of purely gravitational interactions ($\lambda = 0$) is considered.

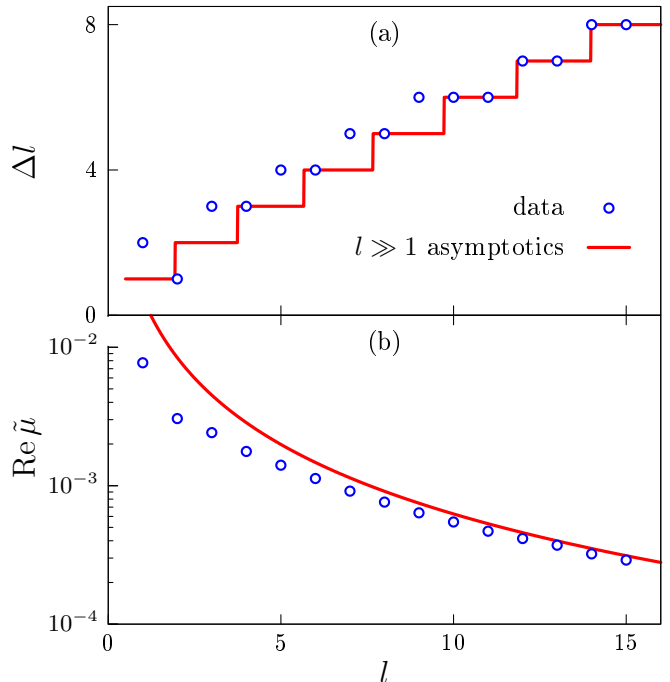


FIG. 5. Parameters of the dominant instability modes in the backgrounds of Bose stars with different l : (a) angular momentum transfers Δl and (b) growth exponents $\text{Re } \mu$ in units of Eq. (3). We consider negligible self-interaction of particles, $\lambda = 0$. Numerical data (circles) rapidly approach large l asymptotics (4) (lines).

linear equation²

$$2\alpha_l + 3/2 + \ln(\beta\alpha_l/l^2) = 0 \quad \text{with} \quad \beta \approx 2.86 \cdot 10^{-2}. \quad (5)$$

Figure 5 shows that Eqs. (4) (lines) approach the numerical data at high angular momenta, though at crude level they are already valid at $l \sim 1$.

The analytic method giving Eqs. (4) is based on a simple observation that the $l \gg 1$ Bose stars have forms of parametrically thin rings with cross-section profiles satisfying a set of ordinary differential equations. We believe

² With numerical solution $\alpha_l \approx \{1.02, 1.51, 1.82, 2.05, 2.23, 2.38, 2.51, 2.62, 2.72, 2.81\}$ at $l = \{1, \dots, 10\}$ and large l asymptotics $\alpha_l = \ln l + O(\ln \ln l)$.

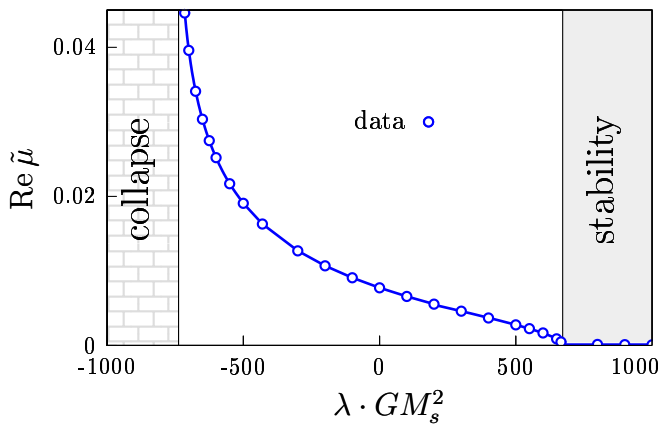


FIG. 6. The fastest instability exponent $\text{Re } \mu$ of the $l = 1$ Bose star as a function of the boson self-coupling λ (line–points) at $M_s = \text{const}$. Units of μ are introduced in Eq. (3). Shaded regions correspond to collapsing stars at large negative λ and absolutely stable stars at $\lambda > \lambda_0$.

that this technique can be generalized to highly nontrivial situations, in particular, to nonzero self-coupling and to the relativistic model of [44–46].

Notably, in model with ultralight (fuzzy) dark matter the lifetimes of unstable rotating Bose stars can formally exceed the age of the Universe. Indeed, in this case Eqs. (3), (4) give,

$$(\text{Re } \mu)^{-1} \simeq 10^{10} \text{ yr} \cdot l^2 \left(\frac{m}{10^{-22} \text{ eV}} \right)^{-3} \left(\frac{M_s}{4 \cdot 10^7 M_\odot} \right)^{-2},$$

where we used $\alpha_l \sim 1$. One may hastily conclude that these configurations are stable on the cosmological timescales if $m \sim 10^{-22} \text{ eV}$, $l \gtrsim 1$, and $M_s \lesssim 4 \cdot 10^7 M_\odot$. But in fact, their lifetimes are always comparable to the oscillation periods $2\pi/\omega_s$ in Eq. (1):

$$|\omega_s|/\text{Re } \mu \approx 1.7(\alpha_l + 1) \sim O(1), \quad (6)$$

where the large l analytics was used, again. Thus, these Bose stars are not the long-living composite objects, as their particles cannot be assigned to the fixed-energy levels $\omega = \omega_s$ of the Bose–Einstein condensates at timescales of order or smaller than $|\omega_s|^{-1}$. In addition, the lifetimes of these rotating objects are shorter than the free-fall times $t_{\text{free}} \sim l/|\omega_s|$ in their gravitational fields and hence much smaller than their nucleation times in reasonable formation mechanisms [7–10, 20]. All of this leaves only one way to observe the rotating Bose stars in simulations: tune the initial data to their profiles with exponential precision, like we did in Fig. 4.

Finally, we investigate numerically (in)stability of the $l = 1$ Bose star in the model with nonzero particle self-interactions. Figure 6 shows the result of this study: dependence of the dominant decay exponent $\text{Re } \mu$ on the self-coupling λ at a given star mass M_s (points and an interpolating line). Notably, the stationary fixed-mass

Bose stars with $l = 1$ exist only at $\lambda > \lambda_{cr}$, where³

$$\lambda_{cr} = (-738 \pm 4)/(GM_s^2). \quad (7)$$

In the case of stronger attraction⁴ (smaller λ) these objects collapse [27], i.e. squeeze towards the higher density regions in a self-similar fashion [26, 28]. This process is shown in the movie [48b].

Figure 6 confirms that the $l = 1$ Bose stars are indeed unstable in the cases of negligibly weak or attractive self-interactions: $\text{Re } \mu > 0$ at $\lambda \leq 0$. This result is in agreement with our no-go theorem. In addition, we see that the instability region extends towards moderately small positive couplings $\lambda < \lambda_0$, where

$$\lambda_0 \approx (672 \pm 2)/(GM_s^2) \quad (8)$$

marks the beginning of the gray region in Fig. 6.

At $\lambda > \lambda_0$, however, our numerical data are consistent⁵ with $\text{Re } \mu \approx 0$. This suggests that the $l = 1$ star is absolutely stable⁶ at large λ , see the movie [48c]. Conversely, this happens at large mass, $M_s \gtrsim 25.9/(G\lambda)^{1/2}$. Thus, the Bose–Einstein condensate behaves more like a solid body if self-repulsion dominates in the equations. The same stabilization effect was previously observed in the relativistic case in [46].

This paper is organized as follows. We introduce rotating Bose stars in Sec. II, prove no-go theorem on their instability in Sec. III, and numerically illustrate decay of the $l = 1$ star in Sec. IV. Then we compute the instability modes of all rotating objects: numerically at moderately small l in Sec. V and analytically at $l \gg 1$ in Sec. VI. In Sec. VII we discuss generalizations of our results.

II. ROTATING BOSE STARS

A system of self-gravitating nonrelativistic bosons is described at large occupation numbers by collective wave function $\psi(t, \mathbf{x})$ and gravitational potential $\Phi(t, \mathbf{x})$. The latter quantities satisfy Gross–Pitaevskii and Poisson equations,

$$i\partial_t \psi = -\frac{\Delta \psi}{2m} + \left(m\Phi + \frac{\lambda|\psi|^2}{8m^2} \right) \psi, \quad (9)$$

$$\Delta \Phi = 4\pi m G |\psi|^2, \quad (10)$$

³ Errorbars in Eqs. (7), (8) are related to numerical errors. They estimate the sensitivities of fits for λ_{cr} and λ_0 to lattice parameters, see Sec. VB for details.

⁴ Or, conversely, at masses above critical $M_{cr}^{(l=1)} \approx 27.2/(-\lambda G)^{1/2}$ in models with $\lambda < 0$. As anticipated in [25, 29], this critical mass exceeds the respective value at $l = 0$, cf. [27, 28].

⁵ More precisely, the numerical procedure formally gives $\text{Re } \tilde{\mu} < 2 \cdot 10^{-4}$ which is below the accuracy of calculations.

⁶ When our work was already completed, a numerical investigation of rotating Bose–Einstein condensed galaxy halos with repulsive particle self-interactions has appeared [49]. The parameters of that study correspond to $\lambda \approx 6 \lambda_0$ — hence, a stable vortex with $l = 1$ was observed.

l	$\tilde{E}_s \cdot 10^3$	l	$\tilde{E}_s \cdot 10^3$	l	$\tilde{E}_s \cdot 10^3$
0	-54.2	1	-19.0	2	-10.3
3	-6.57	4	-4.64	5	-3.49
6	-2.74	7	-2.24	10	-1.34
15	-0.736	$\gg 1 \quad \tilde{E}_s \approx -\alpha_l(\alpha_l + 1)/(8\pi^2 l^2)$			

TABLE II. Energies of the rotating Bose stars at different l in the case $\lambda = 0$; physical units can be restored using Eq. (15). The data with $l \leq 15$ are obtained numerically, while the last item lists large l asymptotics of Sec. V. Parameters α_l obey Eq. (5).

where the extra potential $\lambda|\psi|^2/8m^2$ represents contact self-interaction of bosons with self-coupling⁷ λ . Below we consider all three cases of repulsive, attractive, and negligible self-interactions: $\lambda > 0$, $\lambda < 0$, and $\lambda = 0$. The last two are especially interesting, as they are relevant for the popular dark matter models with QCD axions [50] and ultralight (fuzzy) axion-like particles [6, 8].

One can define the rotating Bose star as a stationary and axially-symmetric solution (1) to the system (9), (10). This means that its wave function $\psi_s(r, z)$ obeys a stationary Schrödinger equation

$$\omega_s \psi_s = -\frac{\Delta \psi_s}{2m} + \left(m\Phi_s + \frac{\lambda|\psi_s|^2}{8m^2} \right) \psi_s, \quad (11)$$

whereas $\Phi = \Phi_s(r, z)$ satisfies Eq. (10). Hereafter we mark all Bose star quantities with the subindex s and keep in mind that axially-symmetric Laplacian $\Delta \psi_s \equiv \partial_z^2 \psi_s + r^{-1} \partial_r (r \partial_r \psi_s) - l^2 \psi_s / r^2$ includes a centrifugal barrier in the last term. Apparently, Eq. (11) describes nonrelativistic particles occupying a single level of their self-made potential well $m\Phi_s + \lambda|\psi_s|^2/8m^2$. All of them have energy ω_s and angular momentum l .

Note that m and G disappear from all equations after coordinate and field rescalings with arbitrary parameter v_0 : $\mathbf{x} = \tilde{\mathbf{x}}/mv_0$, $t = \tilde{t}/mv_0^2$ or $\omega_s = mv_0^2 \tilde{\omega}_s$, $\psi = v_0^2(m/G)^{1/2} \tilde{\psi}$, and $\Phi = v_0^2 \tilde{\Phi}$. We perform numerical calculations in these dimensionless units selecting $v_0 = mGM$ to make the total rescaled mass equal to one: $M = 1$. This leaves only one constant in the equations: the rescaled self-coupling $\tilde{\lambda} = \lambda GM^2$ replacing λ .

Solving Eqs. (10), (11), one obtains Bose stars at different l and $\tilde{\lambda}$; we will gradually introduce relevant numerical and analytic techniques in Secs. IV–VI. All rotating ($l \geq 1$) objects have distinctive toroidal forms, like the one with $l = 1$ and $\lambda = 0$ in Fig. 2.

To investigate (in)stability of these stars, we need another kind of analysis. It is important that the nonrelativistic evolution (9), (10) conserves a number of quanti-

ties: the total mass M and multiplicity N of bosons,

$$M \equiv mN = m \int d^3 \mathbf{x} |\psi|^2, \quad (12)$$

their energy

$$E = \int d^3 \mathbf{x} \left[\frac{|\nabla \psi|^2}{2m} + \frac{m}{2} \Phi |\psi|^2 + \frac{\lambda |\psi|^4}{16m^2} \right], \quad (13)$$

and the components of the net angular momentum, e.g.

$$J_z = -i \int d^3 \mathbf{x} \psi^* \partial_\varphi \psi, \quad (14)$$

where $\varphi = \arctan(y/x)$ is the angular cylindrical coordinate. The values of these integrals characterize the Bose stars. Say, the $l = 1$ star in Fig. 2 has $\tilde{E}_s \approx -0.019$ or, in physical units,

$$E_s = \tilde{E}_s m^2 G^2 M_s^3, \quad (15)$$

where we performed rescaling in Eq. (13). The energies of some Bose stars at $\lambda = 0$ are listed in Table II. Their total spins are proportional to the masses: $J_{z,s} = lM_s/m$, cf. Eqs. (1) and (14).

Now, observe that the Bose stars, rotating or not, extremize the total energy E at a given mass $M = M_s$. In other words, they are the extrema of the functional $F \equiv E - \omega_s N$ where the Lagrange multiplier ω_s fixes $N = M/m$. To show this explicitly, we rewrite the energy (13) in the form

$$E = \int d^3 \mathbf{x} \left[\frac{|\nabla \psi|^2}{2m} + (m\Phi + \lambda u) |\psi|^2 + \frac{(\nabla \Phi)^2}{8\pi G} - 4\lambda m^2 u^2 \right] \quad (16)$$

including the gravitational and self-interaction potentials $\Phi(\mathbf{x})$ and $u(\mathbf{x})$. Once this is done, the functional F reaches extremum at $\Phi = \Phi_s$ and $u = u_s$ satisfying

$$\Delta \Phi = 4\pi G m |\psi|^2 \quad \text{and} \quad u = |\psi|^2 / 8m^2. \quad (17)$$

One can substitute this solution back into Eq. (16) and recover the old energy expression (13). Further variation of F with respect to $\psi^*(\mathbf{x})$ gives the Gross-Pitaevskii equation (11) which together with Eqs. (17) forms the same stationary system for the Bose star profile as before. Thus, rotating Bose stars are indeed the extrema of F labeled with l and M_s .

The question is whether these objects are the local minima of energy at a fixed mass M_s and total spin $J_{z,s}$. In the next Section we will show that at $l \geq 1$ and $\lambda \leq 0$ they are not. Rather, they are the energy saddle points which can be destroyed by an arbitrarily small perturbation growing exponentially with time.

It is worth noting that the above argument identifies ω_s with the binding energy of particles inside the Bose

⁷ Entering as $\lambda a^4/4!$ into the scalar potential of a relativistic field $a(t, \mathbf{x})$.

star, cf. Eq. (1). Indeed, infinitesimally small number of extra particles changes the energy E_s and number N_s of bosons, but not the value of F which is extremal. Thus,

$$dE_s = \omega_s dN_s, \quad (18)$$

i.e. every new particle comes in with energy ω_s . At $\lambda = 0$ this last relation can be combined with Eq. (15) to give

$$\omega_s = 3\tilde{E}_s m^3 G^2 M_s^2 = 3mE_s/M_s, \quad (19)$$

which is useful for numerical tests.

III. NO-GO THEOREM AT $\lambda \leq 0$

Let us prove that rotating Bose stars (1) are unstable at $l \neq 0$ if the self-coupling of their particles is negligible or attractive, $\lambda \leq 0$. These cases are special because at $\lambda \leq 0$ the new energy functional (16) reaches *minimum* with respect to Φ and u at their physical values (17). Thus, we can consider generic independent variations of $\psi(\mathbf{x})$, $\Phi(\mathbf{x})$, and $u(\mathbf{x})$. The Bose star will be proved unstable if one of such variations decreases the energy (16), since physical variation with $\delta\Phi$ and δu provided by Eqs. (17) decreases the energy even further.

We introduce an auxiliary tool: a set of wave functions $\Psi_{l'}(\mathbf{x}) \propto e^{il'\varphi}$ with angular momenta l' satisfying the Schrödinger equation in the Bose star potential (17),

$$\omega_{l'} \Psi_{l'} = -\frac{\Delta \Psi_{l'}}{2m} + (m\Phi_s + \lambda u_s) \Psi_{l'}. \quad (20)$$

For every l' we select the eigenfunction with the minimal $\omega_{l'}$ and normalize it to unity: $\int d^3\mathbf{x} |\Psi_{l'}|^2 = 1$.

Notably, $\Psi_{l'}$ are not the vibrational modes of the Bose star: the latter include related perturbations of ψ , Φ , and u . But Eq. (20) brings in simple quantum mechanical logic which will be useful in what follows. First, at $l' = l$ this equation coincides with Eq. (11) for the condensate profile. Thus, $\omega_l \leq \omega_s$, where strict inequality corresponds to the case of radially excited condensate. Second, and as a consequence of the first, the eigenvalues $\omega_{l'}$ with $l' < l$ are lower than ω_s by a margin because they have weaker centrifugal barriers $l'^2/2mr^2$. In particular, Eqs. (20) with $l' = l$ and $l' = 0$ give,

$$\omega_s - \omega_0 \geq \int d^3\mathbf{x} \frac{l^2 |\Psi_l|^2}{2mr^2} > 0, \quad (21)$$

where we observed that ω_0 is the minimal eigenvalue of the radial Hamiltonian, i.e. the operator in Eq. (20) without the φ derivatives. Third, in the limit $l' \rightarrow \infty$ the eigenfunctions $\Psi_{l'}$ become large in size and therefore interact only with the large- \mathbf{x} asymptotics of the potential $\Phi_s \rightarrow -GM/|\mathbf{x}|$, but not with its short-range part u_s . The respective eigenvalues resemble the ones of the Hydrogen atom: $\omega_{l'} \approx -m^3 G^2 M^2 (l' + 1)^{-2} / 2 \sim O(l'^{-2})$ at $l' \gg 1$.

Now, let us explicitly construct an infinitesimally small deformation that decreases the energy (16) of the original Bose star configuration $\{\psi'_s, \Phi'_s, u'_s\}$ with multiplicity N'_s and winding number $l \geq 1$. First, we extract dN_s particles from the condensate thus obtaining the star $\{\psi_s, \Phi_s, u_s\}$ with $N_s = N'_s - dN_s$ particles and the same winding number. Second, we add back dN_0 particles in the non-rotating state Ψ_0 and $dN_{l'}$ particles in the state $\Psi_{l'}$ with $l' \gg 1$. This process does not modify the total mass and spin if

$$dN_s = dN_0 + dN_{l'} \quad \text{and} \quad l dN_s = l' dN_{l'}. \quad (22)$$

Physically, such deformation corresponds to a simultaneous transition of dN_s condensate particles from the state with angular momentum l to $l' = 0$ and $l' \gg 1$ states.

At the level of configurations, we infinitesimally deform Φ'_s, u'_s to the potentials Φ_s, u_s of the smaller-mass Bose star and change

$$\psi'_s \rightarrow \psi = \psi_s(\mathbf{x}) + dN_0^{1/2} \Psi_0(\mathbf{x}) + dN_{l'}^{1/2} \Psi_{l'}(\mathbf{x}). \quad (23)$$

Substituting Eq. (23) into the expression (16), we obtain the potential energy $E_f \equiv E[\psi, \Phi_s, u_s]$ of this final state:

$$E_f = E_s + \omega_0 dN_0 + \omega_{l'} dN_{l'}, \quad (24)$$

where E_s is the energy of the Bose star with N_s particles and we used Eq. (20) for Ψ_0 and $\Psi_{l'}$. The cross-terms between ψ_s, Ψ_0 , and $\Psi_{l'}$ vanish due to different dependences on φ : recall that $\psi_l \propto e^{il\varphi}$ and $\Psi_{l'} \propto e^{il'\varphi}$, whereas Ψ_0, Φ_s , and u_s are φ -independent.

On the other hand, we started from the Bose star with $N_s + dN_s$ particles and energy

$$E'_s = E_s + \omega_s dN_s + O(dN_s^2), \quad (25)$$

see Eq. (18). Thus, change of the potential energy in the above transition equals

$$E_f - E'_s = (\omega_0 - \omega_s) dN_s + O(l'^{-1}) dN_s < 0, \quad (26)$$

where dN_0 and $dN_{l'}$ were expressed from Eqs. (22) and we recalled that $\omega_{l'} = O(l'^{-2})$. The last inequality follows from Eq. (21). We conclude that the deformation (23) indeed decreases the potential energy of the rotating Bose star.

The above argument proves that all rotating Bose stars are unstable at $\lambda \leq 0$ and arbitrary $l \geq 1$. It also qualitatively identifies the instability mechanism. Namely, the potential energy of the rotating Bose star decreases if some particles perform transitions to nonrotating states and give their angular momenta to other particles going to the periphery of the system. A presumable end-state of this process is a Saturn-like configuration: one or several spin-zero Bose stars surrounded by a rotating cloud of diffuse particles.

A warning is in order. So far we considered an explicit but very non-optimal way of decreasing the Bose star energy. In particular, we voluntarily deformed the

potentials Φ_s , u_s and fixed the angular momenta of the particle end-states. We will see below that the fastest-growing modes represent pairwise transitions of the condensed bosons to the states with angular momenta $l \pm \Delta l$, see Fig. 3.

IV. DECAY OF THE $l = 1$ BOSE STAR

Now, we explicitly visualize the instability of the $l = 1$ Bose star in the model with $\lambda = 0$. We introduce periodic spatial lattice $\{x_n, y_m, z_k\} = \{n\delta, m\delta, k\delta\}$ with uniform spacing δ and fields $\psi_{n,m,k} \equiv \psi(x_n, y_m, z_k)$, $\Phi_{n,m,k}$ sitting on its sites. Since the lattice breaks the rotational symmetry, we will be extra cautious in separating discretization effects from the physical rotational instabilities.

We observe that our cubic lattice is invariant with respect to the $\pi/2$ rotations $\hat{R}_{\pi/2}$ around z axis which map lattice points (x_n, y_m) to $(-y_m, x_n)$ leaving z_k unchanged. From the technical viewpoint, this means that the time evolution in Eqs. (9), (10) commutes with $\hat{R}_{\pi/2}$ even after discretization. On the other hand, the fixed- l configurations (1) are the eigenvalues of these rotations,

$$\hat{R}_{\pi/2} \psi_{n,m,k} \equiv \psi_{-m,n,k} = e^{i\pi l/2} \psi_{n,m,k}. \quad (27)$$

Thus, we define the lattice version of the $l = 1$ Bose star as a minimum-energy configuration satisfying Eq. (27) with the eigenvalue $e^{i\pi/2}$. Such configuration is readily produced by the Euclidean relaxation procedure summarized in Appendix A. At the end of the relaxation, the discretized equations (10), (11) are solved almost exactly, up to negligible round-off errors. The solution is shown in Fig. 2.

It is worth noting that the Bose stars with $l = 1 + 4k$ have the same eigenvalue in Eq. (27) and cannot be separated from the $l = 1$ star on this basis. But their centrifugal barriers are essentially stronger; hence, energy minimization still selects the configuration with $l = 1$. To the contrary, the Bose stars with $l = 0$ and $l = -1$ have the same or smaller energies, but they are excluded by Eq. (27).

Once the Bose star $\psi = \psi_s(\mathbf{x})$ with $l = 1$ is found, we perturb it by adding an asymmetric perturbation,

$$\psi = \psi_s(\mathbf{x}) + A e^{-(r/r_1)^2} \left[\frac{r}{r_1} \cos \varphi + \frac{r^2}{r_1^2} \cos 2\varphi \right] \quad (28)$$

where $\tilde{r}_1 = 10$ and $\tilde{A} = 10^{-8}$ is tiny. Then, evolving Eqs. (9) and (10), we watch the star fall apart. A numerical method for that is described in Appendix A.

The result is shown Fig. 4, see also the movie [48a]. The Bose star remains stationary and toroidal at first. But then it splits into two spherical objects rotating around the mutual center of mass. With time, one of the objects persists and the other gets tidally disrupted. The final configuration includes a non-rotating Bose star surrounded by a cloud of diffuse particles.

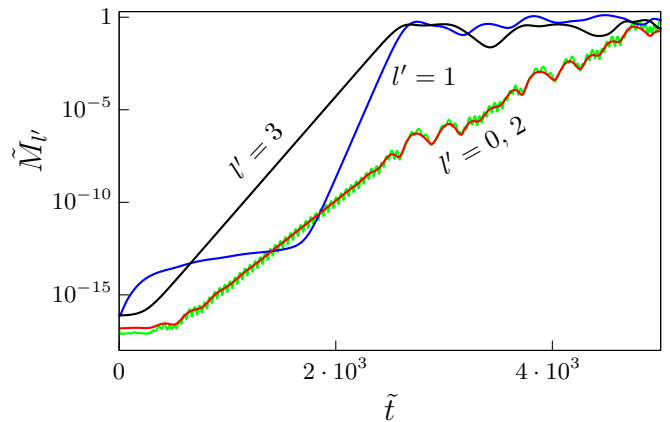


FIG. 7. Norms $M_{l'}(t)$ of the instability modes growing exponentially in the background of the $l = 1$ Bose star. Tildes indicate dimensionless units; $\lambda = 0$.

We stress that the $l = 1$ Bose star is destroyed by the perturbation (28) growing exponentially in its background, not by something else. Without this kick and the round-off errors, it would remain stationary, as its energy is minimal in the sector with fixed $\hat{R}_{\pi/2}$ and the latter operator commutes with the time evolution. We checked that at $A = 0$ the rotating star falls apart at much larger time scales, since initial perturbations in this case are provided by the round-off errors.

To quantify the growing instabilities, we subtract the original Bose star from the numerical solution $\psi(t, \mathbf{x})$ and then split the residual into four parts belonging to the sectors with different eigenvalues of the $\pi/2$ rotations:

$$\psi(t, \mathbf{x}) = \psi_s(\mathbf{x}) e^{-i\omega_s t} + \psi_0 + \psi_1 + \psi_2 + \psi_3. \quad (29)$$

Here $\psi_{l'}(t, \mathbf{x})$ satisfy $\hat{R}_{\pi/2} \psi_{l'} = e^{i\pi l'/2} \psi_{l'}$ at every time t . Roughly speaking, they have angular momenta $l' = 0 \div 3$, although higher l' contributions are also possible. In Appendix A we construct an explicit projector for the decomposition (29).

The norms $M_{l'}(t) \equiv m \int d^3\mathbf{x} |\psi_{l'}|^2$ of the perturbations $\psi_{l'}$ are plotted in Fig. 7. The graphs with $l' = 0, 2, 3$ grow exponentially indicating that their modes are proportional to $\psi_{l'} \propto e^{\mu_{l'} t}$ at the linear stage $\tilde{t} \lesssim 2500$. The perturbation with $l' = 3$ is dominant: it grows faster and becomes nonlinear first. Fitting its graph with the exponent, we obtain $\text{Re } \tilde{\mu}_3 \approx 7.74 \cdot 10^{-3}$ in agreement with the value in Table I which is provided by the axially symmetric method of the next Section. The respective angular momentum transfer equals $\Delta l \equiv |l' - l| = 2$ modulo 4.

The subdominant graphs in Fig. 7 deserve two remarks. First, the norms of ψ_0 and ψ_2 are comparable at all times and $\mu_0 = \mu_2$. We will see below that these perturbations satisfy coupled linear equations and therefore describe the same instability with $\Delta l = |l' - l| = 1$. Second, the graph with $l' = 1$ remains bounded at first and then starts growing with the exponent $\text{Re } \mu_1 \approx 2\text{Re } \mu_3$. This is because the respective perturbation belongs to the same $l = 1$ sector as the Bose star itself and cannot grow

at the linear level. At later times, however, the dominant mode ψ_3 becomes large and starts sourcing $\psi_1 \propto |\psi_3|^2$ via nonlinear terms in the equations.

Since the dominant instability of the $l = 1$ star develops with $\Delta l = |l' - l| = 2$, the respective density perturbation has maxima at two angles: $|\psi_s e^{i\varphi} + \psi_3|^2 - |\psi_s|^2 \propto \cos(2\varphi + \text{const})$. That is why the background star splits into two pieces in Fig. 4c. The subsequent nonlinear evolution in Figs. 7d-f is intricate, however, because the original $l = 1$ star has lower energy than the two isolated nonrotating objects with masses $M_s/2$, see Eq. (15) and Table II. As a consequence, the two half-mass stars remain bound to each other until the perturbations ψ_0 and ψ_2 grow to nonlinearity, too. Once this happens, the bound state gets broken and the final nonrotating object forms, see Fig. 4f.

V. LINEAR INSTABILITIES AT ARBITRARY l

A. No self-interaction

The numerical method of Sec. IV is ideal for visualizing the instability of the $l = 1$ Bose star but it is also not applicable at higher spins. Indeed, fast-rotating objects cannot be separated from their lower l brothers by $\pi/2$ rotations and energy minimization. But nevertheless, we want to compute their instability modes and complex exponents μ . We start with the case of zero self-coupling, $\lambda = 0$.

We compute the stationary profiles $\psi_s(r, z)$, $\Phi_s(r, z)$ of the higher l stars by solving the axially symmetric system (9), (10). To this end we alternate Euclidean time steps for the field ψ with successive overrelaxation (SOR) sweeps for the gravitational potential Φ , see Appendix B for details. The numerical procedure converges to minimal energy configurations with given l – rotating Bose stars. In practice, we use it at moderately large $l = 1 \div 15$. All obtained solutions⁸ have distinctive toroidal forms, see Fig. 8.

The energies of the Bose stars with different l are listed in Table II and visualized in Fig. 9 (points). At large l they approach the analytic expression (line) which will be derived in the next Section.

Next, we perturb the Bose stars to question their stability. A generic perturbation of ψ has arbitrary dependence on φ and therefore includes modes with arbitrary angular momenta l' . One can see, however, that at the linear level the modes with $l' = l + \Delta l$ and $l' = l - \Delta l$ couple to each other but not to other modes. Thus, every such pair can be considered independently, and we write:

$$\begin{aligned} \psi &= [\psi_s(r, z) + \delta\psi e^{i\Delta l\varphi} + \delta\bar{\psi}^* e^{-i\Delta l\varphi}] e^{-i\omega_s t + il\varphi}, \\ \Phi &= \Phi_s(r, z) + \delta\Phi e^{i\Delta l\varphi} + \delta\bar{\Phi}^* e^{-i\Delta l\varphi}, \end{aligned} \quad (30)$$

⁸ Of course, the profile and parameters of the $l = 1$ Bose star coincide with the ones computed in Sec. IV.

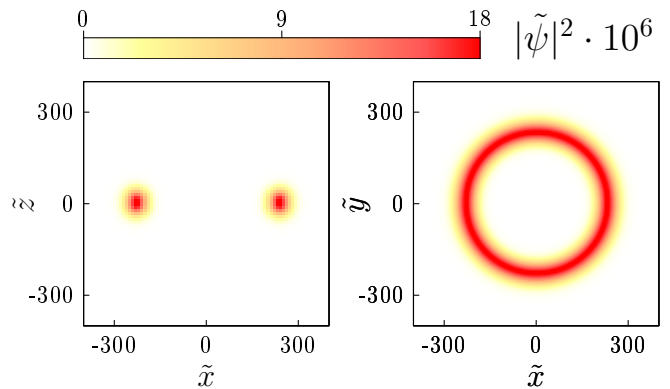


FIG. 8. Rotating Bose star with $l = 10$ and $\lambda = 0$. Dimensionless units of Sec. II are used.

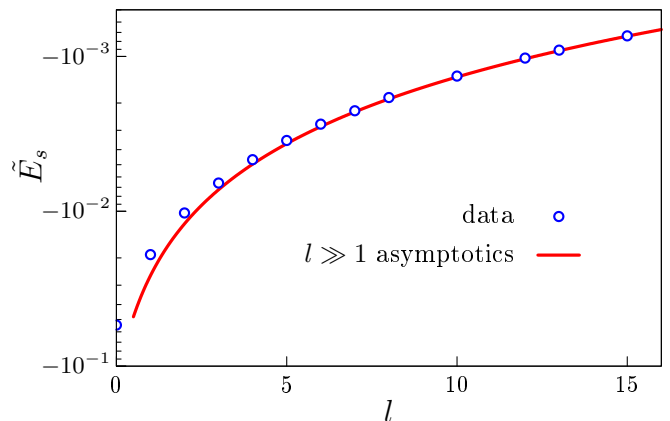


FIG. 9. Energies \tilde{E}_s of the rotating Bose stars at zero boson self-coupling $\lambda = 0$; dimensionless units are introduced in Eq. (15). Points represent numerical data of Sec. V, and the solid line is the analytic large l result of Sec. VI.

where $\delta\psi$, $\delta\bar{\psi}$, and $\delta\Phi$ depend only on r , z , and t .

Substituting Eq. (30) into the Schrödinger–Poisson system (9), (10), we arrive to equations,

$$\begin{aligned} (\omega_s + i\partial_t)\delta\psi &= -\Delta_{r,z}\delta\psi/2m + m\psi_s\delta\Phi \\ &\quad + [(l + \Delta l)^2/(2mr^2) + m\Phi_s] \delta\psi, \\ (\omega_s - i\partial_t)\delta\bar{\psi} &= -\Delta_{r,z}\delta\bar{\psi}/2m + m\psi_s^*\delta\Phi \\ &\quad + [(l - \Delta l)^2/(2mr^2) + m\Phi_s] \delta\bar{\psi}, \\ \Delta_{r,z}\delta\Phi - \Delta l^2\delta\Phi/r^2 &= 4\pi Gm (\psi_s^*\delta\psi + \psi_s\delta\bar{\psi}), \end{aligned} \quad (31)$$

where nonlinear terms in $\delta\psi$, $\delta\bar{\psi}$, $\delta\Phi$ are omitted, and $\Delta_{r,z} \equiv \partial_r^2 + r^{-1}\partial_r + \partial_z^2$ is the radial part of the Laplacian. The last line in Eqs. (31) includes both $\delta\psi$ and $\delta\bar{\psi}$, so they are not independent, indeed. This feature explains, in particular, why the modes with $l' = 0$ and 2 grow with the same exponent in Fig. 7.

To extract the exponentially growing instability modes

$$\delta\psi, \delta\bar{\psi}, \delta\Phi \propto e^{\mu t} \quad \text{with} \quad \text{Re } \mu > 0, \quad (32)$$

we evolve the axially-symmetric equations (31) in real time t using the numerical method of Appendix B. The

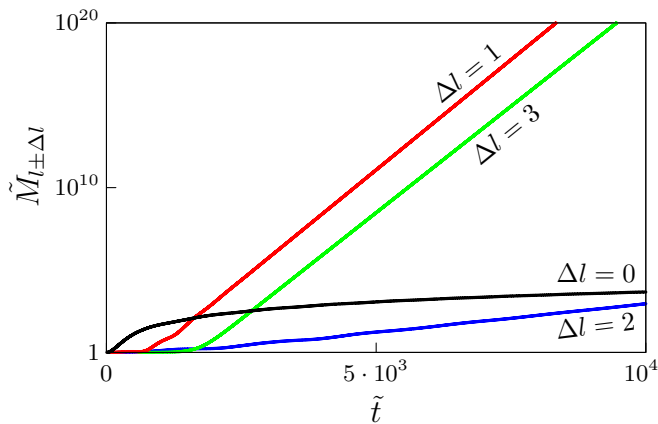


FIG. 10. Norms $M_{l\pm\Delta l}$ (logarithmic scale) of the linear perturbations evolving with time in the background of the $l = 2$ Bose star at $\lambda = 0$.

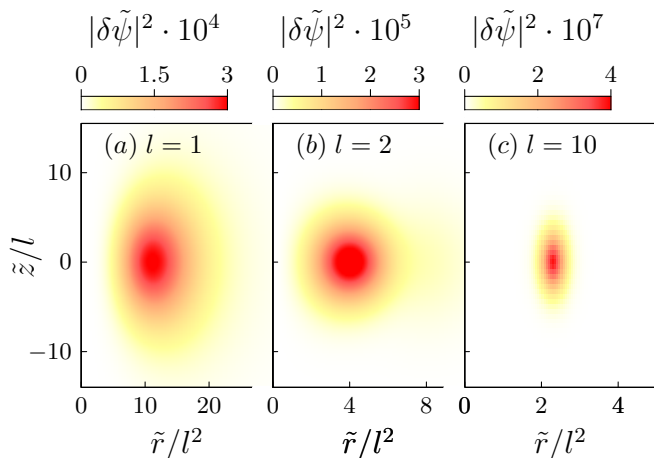


FIG. 11. Dominant instability modes $\delta\psi(r, z)$ of the rotating Bose stars at: (a) $l = 1$, $\Delta l = 2$; (b) $l = 2$, $\Delta l = 1$; and (c) $l = 10$, $\Delta l = 6$. Model with $\lambda = 0$ is considered.

norms $M_{l\pm\Delta l}(t) \equiv m \int d^3x |\delta\psi|^2$ of the perturbations in the background of the $l = 2$ star are shown in Fig. 10. They indeed grow exponentially⁹, as predicted by our no-go theorem.

In practice it is more convenient to keep the perturbations finite. To this end we multiply $\delta\psi$, $\delta\bar{\psi}$, and $\delta\Phi$ by a certain complex factor $\Delta\mathcal{N}$ after every time step. The resulting renormalized solution approaches the profile of the fastest-growing instability mode at large t , while the respective growth exponent equals $\mu = \Delta t^{-1} \ln \Delta\mathcal{N}$.

In Fig. 11 we demonstrate the dominant instability modes of the Bose stars with $l = 1, 2$, and 10 . Like the background stars, they have toroidal forms. The exponents μ and angular momentum transfers Δl of these per-

⁹ The exponents of the graphs with $\Delta l = 1$ and 3 are visibly close, though the one with $\Delta l = 1$ grows faster. This near degeneracy is a peculiarity of the $l = 2$ Bose star.

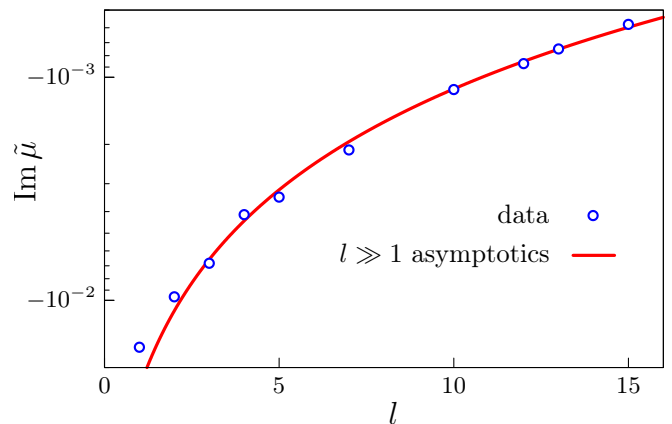


FIG. 12. Imaginary parts of the dominant instability exponents $\text{Im } \mu$ computed in the backgrounds of rotating Bose stars with different l , cf. Fig. 5 and see Eq. (3). We consider negligibly small boson self-coupling $\lambda = 0$. Numerical data (circles) approach the analytic asymptotics (4) (lines) at large l .

turbations are listed in Table I and shown in Figs. 5, 12; see also Eq. (3). These data reproduce the result of the three-dimensional simulations at $l = 1$ and approach analytic expressions of the next Section (solid line) at $l \gg 1$.

B. Self-interacting condensate

Using the procedure of Sec. VA, we compute Bose stars at different nonzero λ . But this time we restrict ourselves to the case $l = 1$. Namely, restoring the last term in Eq. (9), we alternate Euclidean evolution steps $\Delta\tau = i\Delta t$ with renormalizations of ψ and SOR sweeps for Φ in Eq. (10). This gives star configurations with fixed \tilde{M}_s .

Notably, the iterations converge only at $\lambda > \lambda_{cr}$, where the value of the critical coupling $\lambda_{cr} < 0$ was already introduced in Eq. (7). This means that the fixed-mass stationary solutions do not exist at couplings below λ_{cr} (stronger attraction) or, conversely, at a given negative λ and overcritical mass $M_s > M_{cr}^{(l=1)}$. Expressing the mass from Eq. (7), one obtains,

$$M_{cr}^{(l=1)} \approx (27.17 \pm 0.07)/(-G\lambda)^{1/2} \quad (33)$$

at fixed λ .

The overcritical stars do not exist because as one can see numerically, at fixed $\lambda < 0$ the mass M_s grows with $|\omega_s|$ until reaching the maximum $M = M_{cr}^{(l=1)}$ with $dM_s/d\omega_s \approx 0$ cf. [26, 51]. It is clear that analytic continuation to larger $|\omega_s|$ at the other side of the maximum would produce smaller-mass solutions rather than the heavy Bose stars.

The above critical behavior at $M > M_{cr}^{(l=1)}$ is the same as in the case of non-rotating Bose stars [27]. Physically, it is caused by self-attraction dominating in the dense

Bose–Einstein condensate and forcing the objects with large mass to collapse, i.e. squeeze in a self–similar manner [26, 28]. The collapse ends with streams of relativistic bosons leaving the condensate [28]. Due to this process, no stationary Bose stars with given mass exist at $\lambda < \lambda_{cr}$ or $M_s > M_{cr}^{(l=1)}$.

We obtain the value (33) of the critical mass by fitting the fixed- λ numerical data for $M_s(\omega_s)$ with the parabola

$$M_s(\omega_s) \approx M_{cr}^{(l=1)} - c_1(\omega_s - \omega_{cr})^2 \quad (34)$$

in the region $\omega_s \approx \omega_{cr}$, where $M_{cr}^{(l=1)}$, c_1 , and ω_{cr} are the fit parameters. This produces Eq. (33) with errorbars estimating the sensitivity of the fit to the lattice spacing and to the interval of ω_s . Inverting Eq. (33), we get Eq. (7).

Running the three–dimensional simulations of Sec. IV in the model with attractive self–interactions, we explicitly verified that the $l = 1$ Bose star indeed collapses at $\lambda < \lambda_{cr}$, see the movie [48b].

In the opposite case $\lambda > \lambda_{cr}$, we study the Bose star stability by adding self–interaction terms to Eqs. (31) and evolving the perturbations in real time. The norms of $\delta\psi$, $\delta\bar{\psi}$, and $\delta\Phi$ grow exponentially at $\lambda < \lambda_0$, where λ_0 is previewed in Eq. (8). Their exponents $\text{Re } \mu$ are shown in Fig. 6. Thus, in the entire region $\lambda_{cr} < \lambda < \lambda_0$ the Bose star with $l = 1$ decays by shedding off its angular momentum.

The precise value (8) of λ_0 is obtained by fitting the numerical data for $\text{Re } \mu(\lambda)$ with the threshold function

$$\text{Re } \mu = [d_1(\lambda_0 - \lambda) + d_2(\lambda_0 - \lambda)^2]^{1/2} \quad (35)$$

in the region near λ_0 . Like before, the numerical errors are estimated by varying the lattice spacing and interval of λ .

At $\lambda > \lambda_0$, the perturbations remain bounded during the entire real–time evolution. Fitting formally their norms with the exponents, we obtain points in the right–hand side of Fig. 6. The respective values of $\text{Re } \tilde{\mu}$ are all below 2×10^{-4} . In fact, they are smaller than the expected numerical precision and therefore consistent with $\text{Re } \mu \approx 0$, cf. Appendix B. Performing the three–dimensional simulations, we checked that even strongly perturbed star does not decay in this case, see the movie [48c]. We conclude that the $l = 1$ Bose stars are absolutely stable at $\lambda > \lambda_0$ or

$$M > M_0^{(l=1)} \approx 25.9/(G\lambda)^{1/2}, \quad (36)$$

where Eq. (8) was rewritten in terms of mass at a fixed coupling.

VI. ANALYTIC SOLUTIONS AT $l \gg 1$

A. Bose stars

At large l the profiles of rotating Bose stars and their instability modes can be evaluated analytically. Let us

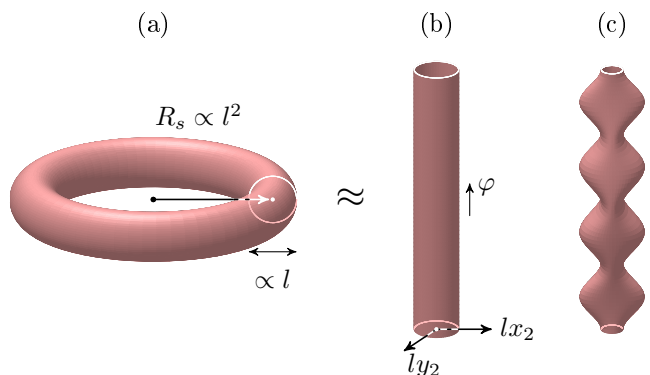


FIG. 13. (Not to scale) (a) Constant density surface of the rotating Bose star at large l . (b) The same for the equivalent object with cylindrical symmetry. (c) Adding the perturbation.

explain the idea of the approximation using crude estimates. In this Section we consider the case of negligible self–coupling, $\lambda = 0$.

The size R_s of the fast–rotating Bose star is large. Indeed, it is determined by balance between the gravitational and centrifugal forces, $|\Phi_s| \sim GM_s/R_s \sim (l/mR_s)^2$, and therefore grows as

$$R_s = 2\pi l^2 / (m^2 GM_s \alpha_l) \propto l^2 \quad (37)$$

at $l \rightarrow +\infty$, where we introduced an order–one parameter α_l . On the other hand, the typical momentum of the condensed bosons is related to the depth of the star potential well: $\Delta_{r,z} \psi_s / \psi_s \sim m^2 \Phi_s \propto l^{-2}$ and hence $\partial_{r,z} \psi_s / \psi_s \propto l^{-1}$. This immediately suggests that the large l star has the form of a ring in Fig. 13a with radius and thickness proportional to l^2 and l , respectively.

The above property is explicit in numerical profiles obtained in the previous Section. Indeed, the object with $l = 10$ in Fig. 8 resembles the torus with two essentially different radii. Naturally, we want to describe such ring–like objects in coordinates $\mathbf{x}_2 = (x_2, y_2)$,

$$r = R_s + lx_2, \quad z = ly_2, \quad (38)$$

which do not depend on l . Recall also that the size $R_s \propto l^2$ of the ring is controlled by the new parameter α_l that will be specified afterwards.

The above observation fixes the l dependence of the binding energy $\omega_s \equiv \omega_2/l^2$ and of the fields,

$$\psi_s = l^{-2} \psi_2(\mathbf{x}_2), \quad \Phi_s = l^{-2} \Phi_2(\mathbf{x}_2) - \frac{l^2}{2m^2 R_s^2}, \quad (39)$$

where we again assumed that the Bose star mass (12) does not depend on l . Substituting the Ansatz (39) into Eqs. (10), (11) and ignoring the terms suppressed by l^{-1} , we arrive at equations for the ring profile,

$$\omega_2 \psi_2 = -\frac{\Delta_2 \psi_2}{2m} + m \Phi_2 \psi_2, \quad (40)$$

$$\Delta_2 \Phi_2 = 4\pi m G |\psi_2|^2. \quad (41)$$

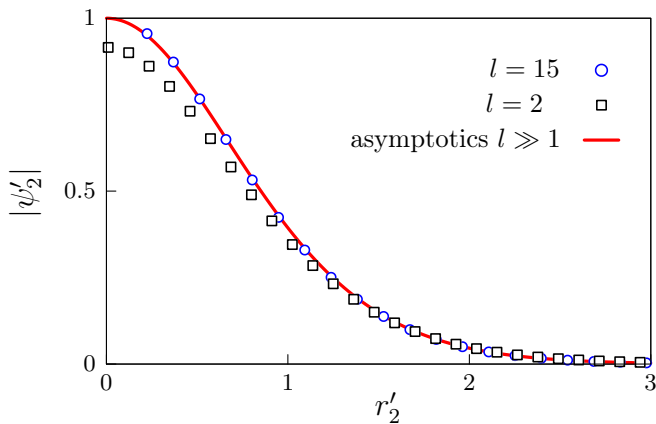


FIG. 14. Two-dimensional Bose star $|\psi_2(r_2)|$ (solid line) versus the sections of the rotating three-dimensional stars $|l^2\psi_s(R_s + lr_2, 0)|$ (points). In the latter case we determine the Bose star radius R_s as a position of the $|\psi_s|$ maximum at $z = \varphi = 0$, then use dimensionless units with parameter v'_0 obtained from Eq. (42). The case $\lambda = 0$ is considered.

Here and below $\Delta_2 \equiv \partial_{x_2}^2 + \partial_{y_2}^2$ is the two-dimensional Laplacian.

Apparently, Eqs. (40), (41) repeat the original Schrödinger–Newton problem (10), (11), but in two dimensions. Thus, the section $\varphi = \text{const}$ of our large l Bose star has the same profile as its nonrotating low-dimensional brother. The extra factor $e^{il\varphi}$ in Eq. (1) ensures rotation.

It is clear now, why all rotating Bose stars are unstable at large l . The radii of their rings are so large that the respective curvature effects do not even contribute into the leading-order equations (40), (41). Hence, these stars are equivalent to the cylindrical objects in Fig. 13b, which can be in turn deprived of the extra-dimensional momentum l by the Galilean transformation. The resulting static configurations of the Bose–Einstein condensate are unstable with respect to decay into many spherical drops with smaller surface tension, see Fig. 13c.

It is natural to expect that the solution of Eqs. (40), (41) has circular symmetry in the \mathbf{x}_2 plane i.e. depends on $r_2^2 \equiv x_2^2 + y_2^2$. As a consequence, the original three-dimensional star is also symmetric, with surfaces of constant density forming flat toruses. We use this property to compute the star profile: substitute $\psi_2 = \psi_2(r_2)$ and $\Phi_2(r_2)$ into Eqs. (40), (41) and solve the resulting ordinary differential equations with the shooting method. This standard calculation is summarized in Appendix C. Notably, the resulting function $\psi_2(r_2)$ is real.

Numerically, it is again convenient to exploit dimensionless units with $G = m = 1$ and restore physical terms afterwards. To this end we rescale $\mathbf{x}_2 = \mathbf{x}'_2/mv'_0$ and $\psi_2 = v_0'^2(m/G)^{1/2}\psi'_2$, $\Phi_2 = v_0'^2\Phi'_2$ like in three dimensions, but with the new parameter v'_0 selected to make $\psi'_2(0) = 1$. The two-dimensional profile $\psi'_2(r'_2)$ is demonstrated in Fig. 14 (solid line). Notably, the sections $\varphi = \text{const}$ of the three-dimensional rotating stars

(points) approach this graph at $l \rightarrow +\infty$.

Given ψ_2 , we calculate the Bose star parameters. Rewriting the integral (12) at large R_s in two-dimensional terms (38), (39) and performing the rescaling, we arrive at the Bose star mass,

$$M_s = \frac{4\pi^2(v'_0)^2 M'_2}{m^2 G^2 M_s \alpha_l}, \quad (42)$$

where we used Eq. (37) and computed the remaining dimensionless integral $M'_2 \equiv \int d^2\mathbf{x}'_2 |\psi'_2|^2 \approx 1.70$. In practice one can use this relation to express the rescaling parameter v'_0 in terms of the total mass M_s . Similarly, the energy (13) of the Bose star equals,

$$E_s = \frac{m^2 G^2 M_s^3}{8\pi^2 l^2} \alpha_l \left[\alpha_l + \frac{1}{2} + \ln(\beta \alpha_l / l^2) \right]. \quad (43)$$

This time we extracted, in addition, v'_0 from Eq. (42) and introduced another numerical coefficient $\beta \approx 2.86 \cdot 10^{-2}$, see Appendix C for details.

We finally extremize the energy (43) with respect to the parameter α_l characterizing the Bose star radius $R_s \propto l^2/\alpha_l$. This gives a nonlinear equation (5) and finishes construction of the large l Bose star. Recall that we already previewed the energy asymptotics (43) in the last element of Table II and in Fig. 9. The last graph roughly agrees with the numerical data even at $l \sim 1$ becoming more precise at larger l . As always, the binding energy of the Bose particles inside the Bose star equals $\omega_s = 3mE_s/M_s$, see Eq. (19).

B. Instabilities

Now, we evaluate exponentially growing modes destroying the fast-rotating Bose stars.

To this end we rescale l from the coordinates and background fields in the linear equations (31) using Eqs. (38), (39). Then, substituting $\delta\psi$, $\delta\bar{\psi}$, $\delta\Phi \propto \exp(\mu t)$, we arrive at the leading-order eigenvalue problem

$$\begin{aligned} -\mu_2 \eta &= \frac{p_\varphi^2 - \Delta_2}{2m} \rho + m\psi_2 \delta\Phi + (m\Phi_2 - \omega_2) \rho, \\ \mu_2 \rho &= \frac{p_\varphi^2 - \Delta_2}{2m} \eta + (m\Phi_2 - \omega_2) \eta, \\ \Delta_2 \delta\Phi &= p_\varphi^2 \delta\Phi + 8\pi G m \psi_2 \rho. \end{aligned} \quad (44)$$

Here we recalled that $\psi_2(\mathbf{x}_2)$ is real and introduced “real” and “imaginary” perturbations $\rho(\mathbf{x}_2) \equiv (\delta\psi + \delta\bar{\psi})/2$ and $\eta(\mathbf{x}_2) \equiv (\delta\psi - \delta\bar{\psi})/2i$. Besides, in Eqs. (44) we traded the angular momentum transfer Δl and complex exponent μ for the parameters

$$p_\varphi = l\Delta l/R_s, \quad \mu_2 = l^2(\mu + ip_\varphi/mR_s). \quad (45)$$

Solving the eigenvalue problem (44), one can find all vibrational modes of the Bose star at a given Δl and determine their exponents μ . Notably, the same problem

with $p_\varphi = 0$ describes vibrations of the two-dimensional star $\psi_2(r_2)$ which is stable. We will therefore focus on the instability modes with $\text{Re } \mu > 0$ at $p_\varphi \neq 0$.

Notably, these exponentially growing perturbations with $\text{Re } \mu > 0$ have several properties proved in Appendix C. First, their eigenvalues μ_2 and profiles ρ , η , $\delta\Phi$ are real. Expectedly so, since Eqs. (44) are real-valued. As a consequence, μ_2 and p_φ parameterize real and imaginary parts of the original exponent μ via Eqs. (45). Second, all instability modes vanish at infinity,

$$\rho, \eta, \delta\Phi \rightarrow 0 \quad \text{as} \quad |\mathbf{x}_2| \rightarrow +\infty. \quad (46)$$

Indeed, less localized solutions of Eqs. (44) describe waves oscillating with real frequencies $i\mu_2$ in the far-away region with $\psi_2 \approx 0$. Third and finally, the instability modes are rotationally-symmetric from the two-dimensional viewpoint, i.e. depend only on $r_2 = |\mathbf{x}_2|$. This last fact agrees with the intuitive figure 13c.

We explicitly compute the profiles of the exponentially growing perturbations using the same strategy as before. Substitute the rotationally invariant Ansatz $\rho(r_2)$, $\eta(r_2)$, $\delta\Phi(r_2)$ into Eqs. (44) and perform rescaling with the parameter v'_0 , e.g. $\rho = v_0'^2(m/G)^{1/2}\rho'(r'_2)$. This gives the system of ordinary differential equations with two dimensionless constants: eigenvalue $\mu'_2 = \mu_2/(mv_0'^2)$ and rescaled extra-dimensional momentum $p'_\varphi = p_\varphi/(mv_0')$. After that apply the shooting method to solve the equations with regularity conditions at the origin and falloff conditions (46) at infinity, see Appendix C for details.

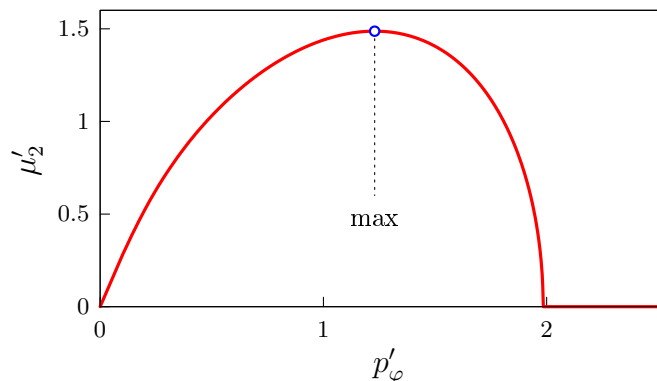


FIG. 15. Eigenvalue μ_2 of the instability mode as a function of the extra-dimensional momentum p_φ .

We find precisely one instability mode at $0 < p'_\varphi < 2$, and no modes outside of this interval. The respective eigenvalue $\mu_2(p_\varphi)$ is plotted in Fig. 15. Since by itself the two-dimensional Bose star is stable, there are no instabilities at $p_\varphi = 0$. In the opposite limit of large p_φ rotational energy makes the operators in the right-hand sides of Eqs. (44) positive-definite and drives μ_2 to negative values.

The fastest-growing perturbation corresponds to the maximum of the graph 15 at $\mu'_2 \approx 1.49$ and $p'_\varphi \approx 1.23$ (point). Rescaling back to physical units and using

Eqs. (45), (37), we obtain real and imaginary parts of the growth exponent μ in Eq. (3) with coefficients

$$\text{Re } \tilde{\mu} = \frac{\mu'_2 \alpha_l}{(2\pi l)^2 M_2'} \approx 2.22 \cdot 10^{-2} \frac{\alpha_l}{l^2}, \quad (47)$$

$$\text{Im } \tilde{\mu} = -\frac{p'_\varphi \alpha_l^{3/2}}{(2\pi l)^2 (M_2')^{1/2}} \approx -2.39 \cdot 10^{-2} \frac{\alpha_l^{3/2}}{l^2}. \quad (48)$$

Besides, the first of Eqs. (45) fixes the angular momentum transfer driving the instability,

$$\Delta l = \left[\frac{l p'_\varphi}{\alpha_l^{1/2} (M_2')^{1/2}} \right] \approx \left[\frac{0.944 \cdot l}{\alpha_l^{1/2}} \right], \quad (49)$$

where $[\cdot]$ denotes the closest integer. Recall that α_l satisfy Eq. (5). We previewed the above asymptotic expressions in Eq. (4) of the Introduction and visualized them in Figs. 5, 12. Let us repeat that the numerical results of Sec. V approach the asymptotic expressions at large l in all figures.

We finish this Section with a forecast on the number of non-spinning Bose stars that can form in the decay of the star with large l . The mass density of the fastest-growing instability mode is proportional to $\cos(\varphi\Delta l + \text{const})$ and therefore has Δl maxima along the ring, see Eqs. (30). Thus, Δl non-spinning objects with mass $M_s/\Delta l$ appear at the first stage of the process, moving in a carousel around the common center. It is instructive to compare their net energy with that of the original Bose star,

$$\frac{E_{s,l}(M_s)}{\Delta l E_{s,0}(M_s/\Delta l)} = \frac{\alpha_l(\alpha_l + 1)\Delta l^2}{8\pi^2 |\tilde{E}_{s,0}| l^2} \approx 0.21(\alpha_l + 1), \quad (50)$$

where the indices and arguments of E_s indicate the mass and angular momentum of the respective Bose star; we used Eqs. (15), (43), (49) and read off $\tilde{E}_{s,0}$ from Table II. Equation (50) implies that the Bose stars with $l \geq 32$ have lower total energy than the chain of Δl non-spinning smaller-mass stars. Thus, the latter objects should remain bound together for some time, like the two-star state in Fig. 4, until — possibly — subdominant instabilities will destroy the chain. On the other hand, some rotating stars with $l < 32$ may directly decay into Δl non-spinning ones.

VII. DISCUSSION

In this paper we analytically proved that rotating non-relativistic Bose stars are unstable at any angular momentum if self-coupling of their bosons is attractive or negligible, $\lambda \leq 0$. This result is relevant for the popular models with QCD axionic or fuzzy dark matter. We also demonstrated that in models with repulsive self-interactions ($\lambda > 0$) the $l = 1$ star is unstable at masses below $M_{s,0} \approx 25.9/(\lambda G)^{1/2}$ and absolutely stable at $M_s > M_{s,0}$, cf. Eq. (8).

We computed the lifetimes of the unstable rotating stars in Eqs. (3) — (6) and in Table I. They are always comparable to the inverse binding energies ω_s^{-1} of the Bose stars and smaller than the free-fall times in their gravitational fields. Thus, the rotating stars (1) cannot nucleate in realistic formation scenarios [7–10, 20] and in fact, cannot be even considered as long-living quasi-stationary states. This observation has a number of phenomenological consequences.

First, the scenario [29] with rotating axion stars reaching threshold for the explosive parametric radioemission [4, 30–33] cannot be realized. One still can consider emission during the intermediate stages when dense and short-living rotating configuration shakes off its angular momentum. But a specific formation scenario for the latter should be suggested in the first place.

Second, instability of rotating Bose stars provides a universal mechanism to destroy the angular momentum. One can imagine e.g. that a subset of dark matter Bose stars collapses gravitationally into black holes with suppressed spins. This is possible in models with positive self-coupling or in axionic models with near-Planckian decay constants [52]. Formation of such non-spinning black holes may explain observational hints in [34–36].

In this paper we also developed an analytic description of fast-rotating Bose stars with $l \gg 1$. This technique is complementary to the numerical methods at moderately small l , it gives parameters and lifetimes of stars as systematic expansions in l^{-1} , cf. Eqs. (4), (43). We saw that such analytics is crudely applicable even at $l \sim 1$, and it becomes precise at higher l , see Figs. 5, 9.

Our analytic method is based on a simple observation that the large l Bose stars have forms of parametrically thin rings, cf. Figs. 8 and 13a. As a consequence, their sections and instability modes can be obtained by solving certain ordinary differential equations. This approach can be easily generalized to nontrivial situations: the case of nonzero self-coupling $\lambda \neq 0$, relativistic model with complex field as in Refs. [44–46], rotating star in the external gravitational potential, etc.

Although the $l = 1$ Bose star becomes stable at sufficiently strong repulsive self-couplings $\lambda > \lambda_0$, Eq. (8), the fate of the higher l objects is far less trivial. In models with dominating self-repulsion the $l \geq 2$ vortices decay [1, 53] into elementary ones with $l = 1$, and the latter spread uniformly over the available volume. This suggests that the axially-symmetric $l \geq 2$ configurations (1) are unstable at any λ , and the real question is whether they decay into gravitationally bound objects with l elementary vortices inside, or most of the vortices migrate to the periphery of the system and disappear in the debris. While this paper was approaching completion, a first study of such process has appeared [49].

Finally, let us remark that although formation of the rotating Bose stars requires fine-tuning of the initial data or a special mechanism, decays of these objects are so complex and aesthetically pleasing that their studies may have a scientific value of their own. Indeed, we expect

higher l stars to break into $\Delta l \propto l$ non-spinning components oscillating and orbiting around the mutual center, cf. the movie [48a]. This state should exist for some time until possibly breaking due to subdominant instabilities. After that some components may tidally disrupt, and the others survive. In the case of attractive self-interactions the component objects may appear overcritical and collapse as bosonova bursting into relativistic axions [28] or photons [33], since they are not protected by the centrifugal barriers anymore.

ACKNOWLEDGMENTS

Instabilities of rotating Bose stars were studied within the framework of the RSF grant 16-12-10494. The rest of this paper was funded by the Foundation for the Advancement of Theoretical Physics and Mathematics “BASIS.” Numerical calculations were performed on the Computational cluster of the Theory Division of INR RAS.

Appendix A: Three-dimensional simulation

In Sec. IV we discuss simulations in three-dimensional box $-L/2 < x, y, z \leq L/2$ with periodic ψ and Φ . Consistency requires modification of Eq. (10) to

$$\Delta\Phi = 4\pi G(m|\psi|^2 - M/L^3), \quad (\text{A1})$$

where the new term with total mass M vanishes as $O(L^{-3})$ in the infinite-volume limit. We discretize x, y , and z with uniform lattice steps $\delta = L/N$ and place the fields $\psi = \psi_{n,m,k}$, $\Phi_{n,m,k}$ on the lattice sites $\{x_n, y_m, z_k\} \equiv \{n\delta, m\delta, k\delta\}$. We perform all calculations in the dimensionless units of Sec. II.

Importantly, our cubic lattice is invariant with respect to $\pi/2$ rotations $\hat{R}_{\pi/2}$. Since $\hat{R}_{\pi/2}^4 = 1$, the latter have four eigenvalues $\pm i$ and ± 1 , and the respective eigenfunctions ψ_l satisfy Eq. (27) with $0 \leq l \leq 3$. In Eq. (29) we decompose $\delta\psi \equiv \psi - \psi_s e^{-i\omega_s t}$ into the sum of eigenfunctions ψ_l using the projectors $\hat{\Pi}_l$,

$$\psi_{l;n,m,k} = \hat{\Pi}_l \delta\psi_{n,m,k} = \frac{1}{4} \left[\delta\psi_{n,m,k} + e^{i\pi l/2} \delta\psi_{m,-n,k} + e^{i\pi l} \delta\psi_{-n,-m,k} + e^{3i\pi l/2} \delta\psi_{-m,n,k} \right]. \quad (\text{A2})$$

The operator $\hat{\Pi}_1$ with $l = 1$ is used in the numerical procedure below.

We evolve the Gross-Pitaevskii-Poisson equations (9), (10) using fourth-order pseudospectral method [9, 54]. In a nutshell, this accounts to performing Fast Fourier Transforms at every time step: first to advance the wave function $\psi(t + \Delta t) = e^{-i\hat{H}\Delta t} \psi(t)$ with precision $O(\Delta t^5)$, then to solve the Poisson equation for the gravitational potential; here \hat{H} is the operator in the right-hand side

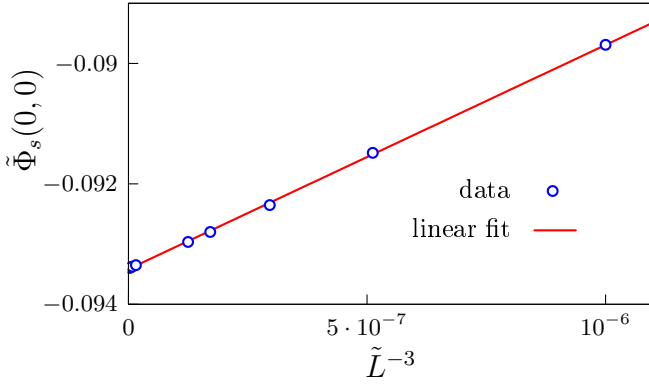


FIG. 16. The potential in the center $r = z = 0$ of the $l = 1$ Bose star as a function of the box size L after the shift by Φ_0 ; the case with no self-interactions is considered.

of Eq. (9). Notably, this numerical scheme equally treats all spatial coordinates and therefore commutes with the $\pi/2$ rotations.

The same evolution in Euclidean time $\tau = it$ multiplies ψ with $e^{-\hat{H}\Delta\tau}$ and therefore minimizes the energy of the configuration. Specifically, in Sec. IV we obtain the $l = 1$ Bose star by iterations $\psi \rightarrow \Delta\mathcal{N}e^{-\hat{H}\Delta\tau}\hat{\Pi}_z\hat{\Pi}_1\psi$, solving the Poisson equation at every step. Here the operator $\hat{\Pi}_1$ projects ψ onto the eigensector of the $\pi/2$ rotations with the eigenvalue $e^{i\pi/2}$, another projector $\hat{\Pi}_z\psi_{n,m,k} \equiv \frac{1}{2}(\psi_{n,m,k} + \psi_{n,m,-k})$ stabilizes the configuration in the z direction by imposing $z \rightarrow -z$ symmetry, Euclidean propagator $e^{-\hat{H}\Delta\tau}$ kills the higher-energy components of ψ , whereas the normalization factor $\Delta\mathcal{N}$ fixes the total mass $\int d^3\tilde{x}|\tilde{\psi}|^2 = 1$ in the rescaled units. At the end of the relaxation the value of ψ equals ψ_s and the normalization factor $\Delta\mathcal{N} = \exp(\tilde{\omega}_s\Delta\tilde{\tau})$ gives the binding energy $\tilde{\omega}_s$.

In the periodic box, it is convenient to fix the constant part of the Bose star potential using condition $\int d^3\mathbf{x}\Phi_s = 0$. We restore the standard terms by shifting $\Phi_s \rightarrow \Phi_s + \Phi_0$ and $\omega_s \rightarrow \omega_s + \Phi_0$, where the constant Φ_0 ensures Virial relation, e.g. $E_s = \omega_s N_s/3$ at $\lambda = 0$. After the shift, the finite-size effects in the energetic quantities reduce to $O(L^{-3})$, see Fig. 16. We do not perform this shift at $\lambda \neq 0$ because it does not affect the data in Fig. 6.

In practice we exploit 128^3 lattice in the $\tilde{L} = 200$ box and use the time steps $\Delta\tilde{t} = \Delta\tilde{\tau} = 0.5$. After 10^4 Euclidean iterations the configuration with $l = 1$ stabilizes at the relative level $\delta\psi_s/\psi_s \sim 10^{-15}$ which is comparable to the round-off errors. The relative effects of the finite lattice spacing δ and discrete time step are of order $2 \cdot 10^{-14}$ and $2 \cdot 10^{-12}$, respectively; they are estimated by using 256^3 lattice and step $\Delta\tilde{\tau} = 0.25$. The largest numerical artifacts come from the finite-volume cutoff: increasing \tilde{L} by a factor of two, we obtain ψ_s with relative corrections of order 10^{-4} .

Next, we add the perturbation (28) to the Bose star and evolve the resulting configuration in real time to

$\tilde{t} = 10^4$. The total energy and mass of the solution are stable during the entire evolution up to relative corrections of order $2 \cdot 10^{-9}$ and $5 \cdot 10^{-11}$, respectively. At the same time, numerical inaccuracies in ψ grow exponentially because the evolution is unstable. Nevertheless, δ and Δt discretization errors always stay below $\delta\psi/\psi < 10^{-7}$ and 10^{-5} , while relative finite-volume errors remain smaller than 10^{-2} at $\tilde{t} \lesssim 9500$ reaching 10% level only at the very end of the simulation.

Appendix B: Axially-symmetric code

To compute the $l \geq 2$ stars numerically, we introduce $N_r \times N_z$ lattice with uniform spacings δ_r, δ_z in axial coordinates r, z . The sites of this lattice $(r_j, z_k) \equiv (j\delta_r, k\delta_z)$ fill a large cylindrical region $0 \leq r_j \leq L_r$ and $0 \leq z_k \leq L_z$ in the upper half of the three-dimensional space. We store the field values $\psi_{j,k} \equiv \psi(r_j, z_k)$ and $\Phi_{j,k}$ on the lattice sites and reconstruct them at $z < 0$ using the symmetry $\psi(r, -z) = \psi(r, z)$, $\Phi(r, -z) = \Phi(r, z)$. We use dimensionless units with $\tilde{m} = \tilde{G} = M_s = 1$ introduced in Sec. II.

The Laplacians in Eqs. (9), (10) are discretized in the standard second-order manner:

$$\begin{aligned} \Delta\psi_{j,k} = & (\psi_{j,k+1} + \psi_{j,k-1} - 2\psi_{j,k})/\delta_z^2 \\ & + (\psi_{j+1,k} + \psi_{j-1,k} - 2\psi_{j,k})/\delta_r^2 \\ & + (\psi_{j+1,k} - \psi_{j-1,k})/(2\delta_r r_j) - l^2\psi_{j,k}/r_j^2, \end{aligned} \quad (\text{B1})$$

where similar expression for $\Delta\Phi_{j,k}$ has no last term. We supply the lattice equations with the regularity conditions at the symmetry axis¹⁰ $r = 0$: $\psi = \partial_r\Phi = 0$ or

$$\psi_{0,k} = 0, \quad \Phi_{-1,k} = \Phi_{1,k}. \quad (\text{B2})$$

Boundary conditions at $z = z_0 = 0$ follow from the $z \rightarrow -z$ reflection symmetry:

$$\psi_{j,-1} = \psi_{j,1}, \quad \Phi_{j,-1} = \Phi_{j,1}. \quad (\text{B3})$$

Finally, we impose relevant falloff conditions at the “infinite” lattice boundaries $r = L_r$ and $z = L_z$. In there, the wave function vanishes,

$$\psi_{j,k} = 0 \quad \text{at} \quad j = N_r - 1 \text{ or } k = N_z - 1, \quad (\text{B4})$$

and the potential is close to the the asymptotics $\Phi \approx -GM/(r^2 + z^2)^{1/2}$. The latter condition can be written in the mass-independent form:

$$\Phi_{N_r-1,k} = \Phi_{N_r-2,k} \left(\frac{r_{N_r-2}^2 + z_k^2}{r_{N_r-1}^2 + z_k^2} \right)^{1/2}, \quad (\text{B5})$$

¹⁰ At $l = 0$ we use $\psi_{-1,k} = \psi_{1,k}$.

and similarly at $z = L_z$ and arbitrary r_j . To sum up, the above discretization gives a set of evolution and Poisson equations at the internal lattice sites with boundary values of the fields fixed by Eqs. (B2) — (B5).

We solve Eq. (10) for $\Phi_{j,k}$ with the standard red–black SOR method [55]. After every relaxation sweep we evolve¹¹ the wave function in Euclidean time by $\Delta\tau = i\Delta t$,

$$\psi_{j,k}^{(n+1)} = \psi_{j,k}^{(n)} - \Delta\tau \hat{H} \psi_{j,k}^{(n)}, \quad (\text{B6})$$

where n indexes the sweeps and \hat{H} denotes the discretized operator in the right–hand side of Eq. (9). Like before, the evolution (B6) kills all excited energy levels in ψ at a given l . Finally, we rescale $\psi_{j,k} \rightarrow \Delta\mathcal{N} \psi_{j,k}$ to keep the total mass $\tilde{M}_s = 1$ fixed and then proceed to the next relaxation sweep. We decrease the time steps from $\Delta\tau \propto \delta_{r,z}$ in the beginning of the relaxation to $\propto \delta_{r,z}^2$ at the end of it.

The iterations converge producing the Bose stars up to corrections $O(\delta_{r,z}^2)$ in lattice steps and¹² $O(L_{r,z}^{-3})$ in box size. Changing the parameters, we numerically confirmed the scalings of the numerical errors with $\delta_{r,z}$ and $L_{r,z}$. The energy of the Bose star is given by the discretized integral (13), while $\tilde{\omega}_s = 3\tilde{E}_s$ at $\lambda = 0$, see Eq. (19).

In practical computations we use lattices ranging between $N_r \times N_z = 101 \times 101$ and 1501×1501 . We enlarge them by a factor of two to control the discretization errors which never exceed $\delta\psi_s/\psi_s < 10^{-2}$. Our box sizes $L_{r,z} \propto l^2$ strongly vary with l to encompass the Bose stars: from $\tilde{L}_r = \tilde{L}_z = 100$ at $l = 1$ to 22500 at $l = 15$. This keeps the relative finite–volume inaccuracies below 10^{-6} . Finally, we ascertain that the axially–symmetric profiles of the $l = 0, 1$ Bose stars coincide with the ones from the three–dimensional code within the expected 1% accuracy.

Once the Bose star is obtained, we evolve Eqs. (31) in real time thus extracting the fastest–growing linear instability mode. We use the same second–order discretization as before and similar boundary conditions to Eqs. (B1) — (B4). Since the real–time evolution is more demanding to computational resources, we exploit smaller lattices in smaller boxes at the cost of lower precision. Now, $N_r \times N_z$ range between 101×101 and 1001×1001 , whereas the box sizes vary within the interval $10^2 \leq \tilde{L}_r, \tilde{L}_z \leq 10^3$. Our time evolution uses Crank–Nicolson steps [55] with $\Delta\tilde{t} = 0.2 \tilde{\delta}_{r,z}^2 / l'^2$. After every step we perform one SOR sweep for the $\delta\Phi$ equation. Then we multiply¹³ $\delta\psi, \delta\bar{\psi}$

and $\delta\Phi$ by a constant $\Delta\mathcal{N}$, and proceed to the next time step. We stop the procedure when the rescaled perturbations stabilize at the relative level 10^{-13} . At the final step we compute the complex exponent of the perturbation: $\tilde{\mu} = \Delta\tilde{t}^{-1} \ln \Delta\mathcal{N}$. Changing l' , we select the dominant mode with maximal $\text{Re} \tilde{\mu}$.

Like before, we estimate numerical precision by varying $N_{r,z}, L_{r,z}$, and Δt . All relative inaccuracies stay below 1%, although this time the largest errors are related to the comparable finite–volume and discretization effects.

Appendix C: Two–dimensional Bose stars

In this Appendix we numerically solve Eqs. (40), (41) for the profile of the two–dimensional Bose star. To this end we absorb ω_2 into the potential,

$$U_2(\mathbf{x}_2) \equiv \Phi_2(\mathbf{x}_2) - \omega_2/m, \quad (\text{C1})$$

introduce radial coordinate $r_2 = |\mathbf{x}_2|$ and perform coordinate and field rescalings with parameter $(v'_0)^2 = (G/m)^{1/2} \psi_2(0)$, as described in Sec. VIA. Our choice of v'_0 fixes the central value of the dimensionless field to $\psi'_2(0) = 1$.

Assuming rotational symmetry, we obtain ordinary differential equations for $\psi'_2(r'_2)$ and $U'_2(r'_2)$,

$$\partial_{r'_2}(r'_2 \partial_{r'_2} \psi'_2) = 2r'_2 U'_2 \psi'_2, \quad (\text{C2a})$$

$$\partial_{r'_2}(r'_2 \partial_{r'_2} U'_2) = 4\pi r'_2 |\psi'_2|^2. \quad (\text{C2b})$$

We supply them with the regularity conditions at the origin,

$$\partial_{r'_2} U'_2(0) = \partial_{r'_2} \psi'_2(0) = 0, \quad \psi'_2(0) = 1, \quad U'_2(0) = U'_0,$$

where $\psi'_2(0) = 1$ follows from the field rescaling and we introduced new parameter U'_0 .

We numerically solve Eqs. (C2) from the above initial data to large r'_2 , and then tune U'_0 to ensure falloff of the wave function at infinity: $\psi'_2 \rightarrow 0$ as $r'_2 \rightarrow +\infty$. This gives $U'_0 \approx -2.07$ and a configuration in Fig. 14 (solid line). After that we compute the dimensionless integral

$$M'_2 \equiv \int d^2 \mathbf{x}'_2 |\psi'_2| \approx 1.7 \quad (\text{C3})$$

in the expression (42) for the Bose star mass.

Let us now apply the above object to find the profile of the fast–rotating three–dimensional Bose star. In two dimensions, the gravitational potential logarithmically grows at infinity,

$$U'_2 \rightarrow M'_2 \ln(r'^2_2 M'_2 / 64\beta), \quad \text{as } r'_2 \rightarrow +\infty, \quad (\text{C4})$$

where the numerical constant $\beta \approx 2.86 \cdot 10^{-2}$ parameterizes its constant part. As a consequence, we cannot separate U_2 into Φ_2 and ω_2 using two–dimensional logic alone.

To do that, we compute the original three–dimensional potential at the spatial point $z = 0$ and $r = R_s + lr_2$

¹¹ Since the Euler formula (B6) is unstable, we upgrade it to a semi–implicit method: replace $\psi_{j,k}^{(n)} \rightarrow \psi_{j,k}^{(n+1)}$ in all diagonal terms of the operator \hat{H} and express $\psi_{j,k}^{(n+1)}$ from the resulting equation.

¹² Because Eq. (B5) ignores the dipole part in the Bose star gravitational potential.

¹³ This renormalization is switched off in Fig. 11.

located parametrically far away from the ring core, $r_2 \gg O(1)$, and yet belonging to the applicability region $r_2 \ll R_s/l$ of Eqs. (C2). In this case the details of the ring profile are indiscernible, and we write

$$\begin{aligned} \Phi_s &\approx -\frac{GM_s}{2\pi} \oint \frac{d\varphi}{\sqrt{4(R_s^2 + lr_2 R_s) \sin^2(\varphi/2) + l^2 r_2^2}} \\ &\approx \frac{GM_s}{\pi R_s} \ln(lr_2/8R_s), \end{aligned} \quad (\text{C5})$$

where the integral in the first line sums up potentials of the ring pieces at different angles φ . Translating the asymptotics (C4) of U'_2 to physical units and substituting it into Eqs. (C1), (39), we obtain another expression for Φ_s which should coincide with Eq. (C5). This gives,

$$\omega_s = \frac{l^2}{2mR_s^2} + \frac{mGM_s}{2\pi R_s} \ln(\beta\alpha_l/l^2), \quad (\text{C6})$$

where we traded R_s for α_l using Eq. (37).

Finally, let us compute the energy E_s of the three-dimensional Bose star at large l . Its analog in two dimensions has the form,

$$\begin{aligned} \mathcal{E}_2 &= \int d^2\mathbf{x}_2 \left(\frac{|\nabla_{\mathbf{x}_2} \psi_2|^2}{2m} + \frac{m}{2} U_2 |\psi_2|^2 \right) \\ &= K_2 + P_2. \end{aligned} \quad (\text{C7})$$

where K_2 and P_2 are the kinetic and potential terms, respectively. The two-dimensional Bose star $\psi_2 = \psi_{2,s}(\mathbf{x}_2)$ extremizes this functional in the class of configurations with a given mass $M_2 \equiv \int d^2\mathbf{x}_2 m |\psi_2|^2$, cf. Sec. II. In particular, rescaling

$$\psi_2'' = \gamma \psi_{2,s}(\gamma \mathbf{x}_2), \quad U_2'' = U_{2,s}(\gamma \mathbf{x}_2) - 2GM_{2,s} \ln \gamma, \quad (\text{C8})$$

does not change the mass and large r_2 asymptotics of the potential U_2 . Thus, the energy (C7) of the rescaled configuration

$$\mathcal{E}_2'' = \gamma^2 K_{2,s} + P_{2,s} - GM_{2,s}^2 \ln \gamma, \quad (\text{C9})$$

is extremal at $\gamma = 1$; hereafter we mark the quantities evaluated for $\psi_2 = \psi_{2,s}$ with the subindex s . Taking the γ derivative, we find $2K_{2,s} = GM_{2,s}^2$ and therefore the two-dimensional Virial theorem

$$\mathcal{E}_{2,s} = K_{2,s}/2 = GM_{2,s}^2/4, \quad (\text{C10})$$

where the first equality is obtained by integrating Eq. (C7) by parts and using Eq. (40).

At large l and $\lambda = 0$ the energy (13) of the three-dimensional Bose star takes the form,

$$E_s = \frac{2\pi R_s}{l^4} \mathcal{E}_{2,s} + \frac{\pi R_s}{ml^2} \left(\omega_s + \frac{l^2}{2mR_s^2} \right) M_{2,s}, \quad (\text{C11})$$

where Eqs. (C1), (C7) were used. We express $\mathcal{E}_{2,s}$ and ω_s from Eqs. (C10) and (C6), write the two-dimensional mass as $M_{2,s} = l^2 M_s / (2\pi R_s)$, and use representation (37) of R_s . This gives the energy expression (43) from the main text.

Once this is done, equation (5) for α_l is obtained by extremizing the energy with respect to this free parameter. Formula (C6) for ω_s then reduces to the expression

$$\omega_s = -\frac{3m^3 G^2 M_s^2}{8\pi^2 l^2} \alpha_l (\alpha_l + 1)$$

which was used in the estimate (6). Notably, the value of ω_s/m coincides with the derivative dE_s/dM_s , as it should.

Appendix D: Instability modes at $l \gg 1$

Now, consider exponentially growing modes in the background of the three-dimensional, fast-rotating Bose star. In the main text we argued that their profiles $\rho(\mathbf{x}_2)$, $\eta(\mathbf{x}_2)$, $\delta\Phi(\mathbf{x}_2)$ satisfy the two-dimensional eigenvalue problem (44). The latter is similar to the problem describing vibrations of the two-dimensional star, but includes an additional parameter: the extra-dimensional momentum p_φ .

For a start, we prove the properties of Eqs. (44) previewed in the main text. These equations constitute a Hamiltonian system for the field $\rho(\mathbf{x}_2)$ and its canonical momentum $\eta(\mathbf{x}_2)$. Indeed, in terms of the phase-space coordinate $\xi(\mathbf{x}_2) = (\rho, \eta)^T$ the equations read,

$$\mu_2 \Omega \xi = \begin{pmatrix} \hat{H}_\rho & 0 \\ 0 & \hat{H}_\eta \end{pmatrix} \xi, \quad \Omega = \begin{pmatrix} 0 & -1 \\ 1 & 0 \end{pmatrix}, \quad (\text{D1})$$

where μ_2 replaces the time derivative, Ω is a canonical form, and real symmetric operators \hat{H}_ρ and \hat{H}_η represent variations of the quadratic Hamiltonian. It is well-known [56] that the solutions of stationary Hamiltonian systems like Eq. (D1) have only purely imaginary or real eigenvalues μ_2 .

Let us demonstrate this explicitly. The operators in Eqs. (44) have forms,

$$\hat{H}_\eta = \frac{p_\varphi^2 - \Delta_2}{2m} + mU_2, \quad \hat{H}_\rho = \hat{H}_\eta + \psi_2 \frac{8\pi Gm^2}{\Delta_2 - p_\varphi^2} \psi_2,$$

where U_2 is the shifted background potential in Eq. (C1). One can explicitly check that these operators are real symmetric, i.e. satisfy the relations

$$\int d^2\mathbf{x}_2 f_1 \hat{H}_{\rho,\eta} f_2 = \int d^2\mathbf{x}_2 f_2 \hat{H}_{\rho,\eta} f_1 \quad (\text{D2})$$

for any well-localized functions $f_1(\mathbf{x}_2)$ and $f_2(\mathbf{x}_2)$. Besides, \hat{H}_η is positive-definite because its eigenvalues measure (non-negative) difference between the energy levels in the potential $\Phi_2(\mathbf{x}_2)$ and its ground-state energy ω_2 , plus a positive constant $p_\varphi^2/2m$. As a consequence, \hat{H}_η and \hat{H}_ρ can be simultaneously diagonalized by a real operator \hat{A} ,

$$\hat{A} \hat{H}_\eta \hat{A}^T = \hat{I}, \quad \hat{A}^{-1T} \hat{H}_\rho \hat{A}^{-1} = \text{diag}(-\mu_j^2), \quad (\text{D3})$$

where \hat{I} is a unity operator and all μ_j^2 are real. Given Eq. (D3), we construct a symplectic operator

$$\hat{S} = \begin{pmatrix} \hat{A}^{-1} & 0 \\ 0 & \hat{A}^T \end{pmatrix}, \quad \hat{S}^T \Omega \hat{S} = \Omega$$

diagonalizing the entire boundary value problem (D1). Indeed, the transformed perturbation $\xi' = \hat{S}^{-1}\xi$ satisfies the diagonal Hamiltonian equations (D1), with operators \hat{I} and $\text{diag}(-\mu_j^2)$ replacing \hat{H}_η and \hat{H}_ρ . Solving the diagonal equations, one finds out that every pair of elements in ξ' represents the “coordinate” and “momentum” of an eigenmode with real $\mu_2^2 = \mu_j^2$. Finally transforming to the original terms, one obtains a complete set of eigenmodes satisfying Eqs. (44). The latter modes are real by construction and their eigenvalues μ_2 are either real or imaginary.

It is clear that all modes located far away from the two-dimensional Bose star have imaginary μ_2 . In this region $\psi_2 \approx 0$, and therefore

$$-\mu_2^2 \eta \approx [(p_\varphi^2 - \Delta_2)/2m + mU_2]^2 \eta,$$

see Eqs. (44). Hence, $\mu_2^2 < 0$. Conversely, all modes with real μ_2 are localized within the domain of nonzero ψ_2 .

To sum up, we proved that all instability modes have real profiles satisfying the falloff conditions (46) at infinity. They can be numerically computed using the standard shooting method. Performing the rescaling with the parameter v'_0 , we get rid of m and G , see Sec. VIA for details. Since the two-dimensional background depends only on the radius $r'_2 = |\mathbf{x}'_2|$, we assume generic separable dependence of perturbations on the angular coordinate $\varphi_2 \equiv \arctan(y'_2/x'_2)$,

$$\rho', \eta', \delta\Phi' \propto \cos(l_2\varphi_2 + \text{const}).$$

This turns Eqs. (44) into a set of ordinary differential equations

$$\begin{aligned} \partial_{r'_2}(r'_2 \partial_{r'_2} \rho') &= 2\mu_2^2 r'_2 \eta' + \rho' [r'_2 (p'_\varphi)^2 + l_2^2/r'_2 + 2U_2 r'_2] \\ &\quad + 2r'_2 \psi_2' \delta\Phi', \\ \partial_{r'_2}(r'_2 \partial_{r'_2} \eta') &= -2\mu_2^2 r'_2 \rho' + \eta' [r'_2 (p'_\varphi)^2 + l_2^2/r'_2 + 2U_2 r'_2], \\ \partial_{r'_2}(r'_2 \partial_{r'_2} \delta\Phi') &= \delta\Phi' [r'_2 (p'_\varphi)^2 + l_2^2/r'_2] + 8\pi r'_2 \psi_2' \rho' \end{aligned}$$

for the radial mode profiles $\Xi(r'_2) = (\rho', \eta', \delta\Phi')$ in dimensionless units with primes.

Next, we solve the equations with regularity conditions at the origin,

$$\partial_{r'_2} \Xi = 0 \quad \text{at} \quad r'_2 = 0, \quad (\text{D4})$$

and falloff conditions (46) at infinity. To this end we construct a complete set of initial data by adding to Eq. (D4)

the condition $\Xi = (1, 0, 0)$ at $r'_2 = 0$, and then do the same for $\Xi = (0, 1, 0)$ and $(0, 0, 1)$. Starting with these three sets of data, we numerically obtain three linearly independent solutions $\Xi^{(1)}(r'_2)$, $\Xi^{(2)}(r'_2)$, and $\Xi^{(3)}(r'_2)$ of

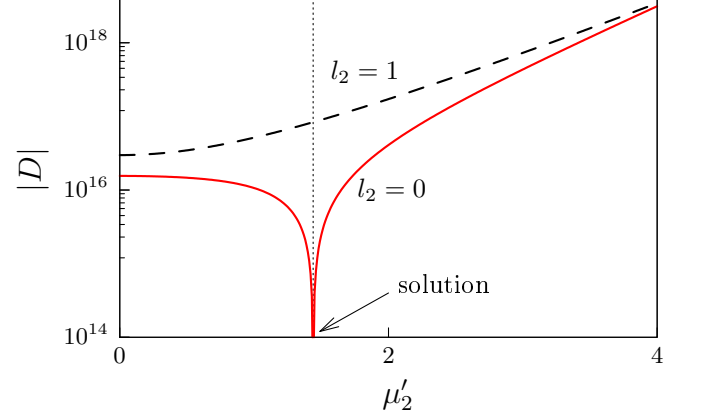


FIG. 17. Absolute value of the determinant (D6) (logarithmic scale) as a function of the eigenvalue μ_2' at $p'_\varphi = 1$, $r'_{\text{max}} = 7$, and $l_2 = 0, 1$. The solution $D = 0$ (vertical dotted line) corresponds to a sharp beak-like dip of the $l_2 = 0$ graph.

the differential equations. General solution is their linear combination:

$$\Xi(r'_2) = d_1 \Xi^{(1)}(r'_2) + d_2 \Xi^{(2)}(r'_2) + d_3 \Xi^{(3)}(r'_2). \quad (\text{D5})$$

The unknown instability mode is given by the combination satisfying, in addition, the falloff conditions (46) at infinity — or, in numerical approximation, equalities $\Xi(r'_{\text{max}}) = 0$ at sufficiently large radius $r'_2 = r'_{\text{max}}$. Together with Eq. (D5) this gives a system of linear algebraic equations for d_i with zero right-hand side. The solution exists only if the coefficient matrix has zero determinant,

$$D = \det [\Xi^{(1)} \Xi^{(2)} \Xi^{(3)}] = 0 \quad \text{at} \quad r'_2 = r'_{\text{max}}, \quad (\text{D6})$$

where the 3×3 matrix under the determinant includes the columns $\Xi^{(i)}(r'_{\text{max}})$. Equation (D6) selects the values of μ_2' representing the instability modes.

In Fig. 17 we show the absolute value of the determinant D as a function of μ_2' at $r'_{\text{max}} = 7 \gg 1$ and $p'_\varphi = 1$. We consider the cases $l_2 = 0$ and 1 (solid and dashed lines, respectively). The sharp dip of the $l_2 = 0$ graph at $\mu_2' \approx 1.44$ indicates the point $D = 0$ and thus the instability mode. At the same time, graphs with $l_2 \geq 1$ do not have zeros of D at all, see the dashed line. This means that the unstable mode is rotationally symmetric in two dimensions, like we claimed in the main text.

Solving Eq. (D6) at all possible values of p'_φ and $l_2 = 0$, we obtain the eigenvalue $\mu_2'(p'_\varphi)$ of the instability mode shown in Fig. 15. The maximum of this graph represents the fastest-growing mode considered in the main text.

-
- [1] L. Landau and E. Lifshitz, *Course of Theoretical Physics, vol. 9 "Statistical Physics: Theory of the Condensed State" by E.M. Lifshitz and L.P. Pitaevskii* (Butterworth-Heinemann, 1980).
- [2] D. J. Kaup, *Phys. Rev.* **172**, 1331 (1968).
- [3] R. Ruffini and S. Bonazzola, *Phys. Rev.* **187**, 1767 (1969).
- [4] I. Tkachev, *Soviet Astronomy Letters* **12**, 305 (1986).
- [5] A. H. Guth, M. P. Hertzberg, and C. Prescod-Weinstein, *Phys. Rev. D* **92**, 103513 (2015), arXiv:1412.5930.
- [6] J. C. Niemeyer, *Prog. Part. Nucl. Phys.* **113**, 103787 (2020), arXiv:1912.07064.
- [7] E. Seidel and W.-M. Suen, *Phys. Rev. Lett.* **72**, 2516 (1994), arXiv:gr-qc/9309015.
- [8] H.-Y. Schive, T. Chiueh, and T. Broadhurst, *Nature Phys.* **10**, 496 (2014), arXiv:1406.6586.
- [9] D. Levkov, A. Panin, and I. Tkachev, *Phys. Rev. Lett.* **121**, 151301 (2018), arXiv:1804.05857.
- [10] B. Eggemeier and J. C. Niemeyer, *Phys. Rev. D* **100**, 063528 (2019), arXiv:1906.01348.
- [11] C. Hogan and M. Rees, *Phys. Lett. B* **205**, 228 (1988).
- [12] E. W. Kolb and I. I. Tkachev, *Phys. Rev. D* **49**, 5040 (1994), arXiv:astro-ph/9311037.
- [13] E. W. Kolb and I. I. Tkachev, *Phys. Rev. Lett.* **71**, 3051 (1993), arXiv:hep-ph/9303313.
- [14] A. Vaquero, J. Redondo, and J. Stadler, *JCAP* **04**, 012 (2019), arXiv:1809.09241.
- [15] M. Buschmann, J. W. Foster, and B. R. Safdi, *Phys. Rev. Lett.* **124**, 161103 (2020), arXiv:1906.00967.
- [16] B. Eggemeier, J. Redondo, K. Dolag, J. C. Niemeyer, and A. Vaquero, *Phys. Rev. Lett.* **125**, 041301 (2020), arXiv:1911.09417.
- [17] M. Gorghetto, E. Hardy, and G. Villadoro, *SciPost Phys.* **10**, 050 (2021), arXiv:2007.04990.
- [18] H.-Y. Schive, M.-H. Liao, T.-P. Woo, S.-K. Wong, T. Chiueh, T. Broadhurst, and W.-Y. P. Hwang, *Phys. Rev. Lett.* **113**, 261302 (2014), arXiv:1407.7762.
- [19] J. Veltmaat, J. C. Niemeyer, and B. Schwabe, *Phys. Rev. D* **98**, 043509 (2018), arXiv:1804.09647.
- [20] J. Chen, X. Du, E. W. Lentz, D. J. Marsh, and J. C. Niemeyer, arXiv:2011.01333.
- [21] V. Silveira and C. M. de Sousa, *Phys. Rev. D* **52**, 5724 (1995), arXiv:astro-ph/9508034.
- [22] F. D. Ryan, *Phys. Rev. D* **55**, 6081 (1997).
- [23] F. E. Schunck and E. W. Mielke, *Phys. Lett. A* **249**, 389 (1998).
- [24] S. Davidson and T. Schwetz, *Phys. Rev. D* **93**, 123509 (2016), arXiv:1603.04249.
- [25] M. P. Hertzberg and E. D. Schiappacasse, *JCAP* **08**, 028 (2018), arXiv:1804.07255.
- [26] V. E. Zakharov and E. A. Kuznetsov, *Physics-Uspekhi* **55**, 535 (2012).
- [27] P.-H. Chavanis, *Phys. Rev. D* **84**, 043531 (2011), arXiv:1103.2050.
- [28] D. Levkov, A. Panin, and I. Tkachev, *Phys. Rev. Lett.* **118**, 011301 (2017), arXiv:1609.03611.
- [29] M. P. Hertzberg and E. D. Schiappacasse, *JCAP* **11**, 004 (2018), arXiv:1805.00430.
- [30] M. P. Hertzberg, Y. Li, and E. D. Schiappacasse, *JCAP* **07**, 067 (2020), arXiv:2005.02405.
- [31] M. A. Amin and Z.-G. Mou, (2020), 10.1088/1475-7516/2021/02/024, arXiv:2009.11337.
- [32] M. A. Amin, A. J. Long, Z.-G. Mou, and P. M. Saffin, (2021), arXiv:2103.12082.
- [33] D. Levkov, A. Panin, and I. Tkachev, *Phys. Rev. D* **102**, 023501 (2020), arXiv:2004.05179.
- [34] B. P. Abbott *et al.* (LIGO Scientific, Virgo), *Phys. Rev. X* **9**, 031040 (2019), arXiv:1811.12907.
- [35] B. P. Abbott *et al.* (LIGO Scientific, Virgo), *Astrophys. J. Lett.* **882**, L24 (2019), arXiv:1811.12940.
- [36] R. Abbott *et al.* (LIGO Scientific, Virgo), arXiv:2010.14529.
- [37] B. Schwabe, J. C. Niemeyer, and J. F. Engels, *Phys. Rev. D* **94**, 043513 (2016), arXiv:1606.05151.
- [38] M. A. Amin and P. Mocz, *Phys. Rev. D* **100**, 063507 (2019), arXiv:1902.07261.
- [39] L. Hui, J. P. Ostriker, S. Tremaine, and E. Witten, *Phys. Rev. D* **95**, 043541 (2017), arXiv:1610.08297.
- [40] X. Du, B. Schwabe, J. C. Niemeyer, and D. Bürger, *Phys. Rev. D* **97**, 063507 (2018), arXiv:1801.04864.
- [41] D. J. Marsh and J. C. Niemeyer, *Phys. Rev. Lett.* **123**, 051103 (2019), arXiv:1810.08543.
- [42] X. Li, L. Hui, and T. D. Yavetz, *Phys. Rev. D* **103**, 023508 (2021), arXiv:2011.11416.
- [43] H.-Y. Schive, T. Chiueh, and T. Broadhurst, *Phys. Rev. Lett.* **124**, 201301 (2020), arXiv:1912.09483.
- [44] N. Sanchis-Gual, F. Di Giovanni, M. Zilhão, C. Herdeiro, P. Cerdá-Durán, J. Font, and E. Radu, *Phys. Rev. Lett.* **123**, 221101 (2019), arXiv:1907.12565.
- [45] F. Di Giovanni, N. Sanchis-Gual, P. Cerdá-Durán, M. Zilhão, C. Herdeiro, J. A. Font, and E. Radu, *Phys. Rev. D* **102**, 124009 (2020), arXiv:2010.05845.
- [46] N. Siemonsen and W. E. East, *Phys. Rev. D* **103**, 044022 (2021), arXiv:2011.08247.
- [47] L. Visinelli, S. Baum, J. Redondo, K. Freese, and F. Wilczek, *Phys. Lett. B* **777**, 64 (2018), arXiv:1710.08910.
- [48] Movies showing three-dimensional numerical evolution of the $l = 1$ rotating Bose star: (a) its decay into a nonrotating object in the model with $\lambda = 0$, see also Fig. 4; (b) collapse at $\lambda < \lambda_{cr}$; (c) stable oscillations of strongly perturbed star in the case $\lambda > \lambda_0$, <https://www.youtube.com/playlist?list=PLMxQF3HFStX2o2ocew9aS6GoQtszIbiT5> (2021).
- [49] Y. O. Nikolaieva, A. O. Olashyn, Y. I. Kuriatnikov, S. I. Vilchynskii, and A. I. Yakimenko, arXiv:2103.07856.
- [50] G. Grilli di Cortona, E. Hardy, J. Pardo Vega, and G. Villadoro, *JHEP* **01**, 034 (2016), arXiv:1511.02867.
- [51] N. Vakhitov and A. Kolokolov, *Radiophys. Quantum Electron.* **16**, 783 (1971).
- [52] T. Helfer, D. J. E. Marsh, K. Clough, M. Fairbairn, E. A. Lim, and R. Becerril, *JCAP* **03**, 055 (2017), arXiv:1609.04724.
- [53] E. Nugaev and A. Shkerin, *Phys. Rev. D* **90**, 016002 (2014), arXiv:1404.3207.
- [54] H. Yoshida, *Phys. Lett. A* **150**, 262 (1990).
- [55] W. Press, S. Teukolsky, W. Vetterling, and B. Flannery, *Numerical Recipes: The Art of Scientific Computing*, 3rd ed. (Cambridge University Press, 2007).
- [56] V. I. Arnold, *Mathematical Methods of Classical Mechanics* (New York: Springer-Verlag, 1989).